Physics of Particles and Nuclei, Vol. 32, No. 6, 2001, pp. 1–33. Translated from Fizika Elementarnykh Chastits i Atomnogo Yadra, Vol. 32, No. 6, 2001, pp. @@–@@.

EXAFS Spectroscopy at Synchrotron-Radiation Beams

V. L. Aksenov*, A. Yu. Kuzmin, J. Purans**, and S. I. Tyutyunnikov***
Kurchatov Institute of Atomic Energy

Abstract—Development of the specialized synchrotron radiation (SR) sources of high brightness affords considerable advancement in using absorption-spectroscopy methods for determining the local atomic and electronic structure of absorbing centers in materials science, physics, chemistry, and biology. This review presents the basic theoretical principles of extended x-ray absorption fine structure (EXAFS) spectroscopy, which is one of the mainstream directions of absorption spectroscopy and allows high-accuracy determination of the parameters of the short-range order in multicomponent amorphous and quasicrystalline substances. Methods of analyzing EXAFS spectra with allowance for multiple-scattering effects are described along with experimental procedures implementing EXAFS spectroscopy at SR beams and requirements to the monochromatization of the radiation beam. An energy-dispersive spectrometer, which can provide the time resolution 3-5 ms, is under development at the SR beam at Kurchatov Institute for studying phase transitions and external actions to an object. The EXAFS-spectroscopy results for oxide compounds of tungsten and molybdenum, whose valence varies in dependence of external actions, are presented. One of the structural problems of the physics of fullerenes-temperature dependence of the position of metal atoms-is successfully solved by using EXAFS spectroscopy.

CONTENTS

1. INTRODUCTION

During the last 15 years, x-ray absorption spectroscopy (XAS) has found extensive application in determining the local atomic and electronic structure of the absorbing centers (atoms) in the materials science, physics, chemistry, biology, and geophysics. Rapid advance in the XAS method is caused by appearance of synchrotron sources all over the world, as well as by considerable achievement in the theory and its practical realization in convenient and easily available software packages [1]. XAS can provide information that substantially complements the results of other experimental methods, such as the diffraction (scattering) of x-rays and neutrons, photoelectron, and emission x-ray spectroscopy. The basic XAS advantages are (i) selectivity in the chemical-element type (in some cases, also in the location of an element in a material), which enables one to acquire information on pair and multiatomic distribution functions for the local environment of each elements of the material under investigation; (ii) sensitivity to the partial densities of vacant states near the Fermi level; (iii) high density sensitivity (10–100 particles per mole) and relatively short times (from milliseconds to tens of minutes) of detecting experimental spectra when the synchrotron radiation is used; and (iv) a small required sample volume (usually, an amount less than 30 mg/cm^2 is enough). Due to these advantages, the employment of XAS is especially attractive for studying the crystalline and disordered (amorphous, glassy, liquid, and gaseous) multicomponent materials, as well as for carrying out *in situ* investigations of dynamical processes (phase transitions and chemical reactions).

When x-rays of energies close to the electron binding energies are absorbed, features known as absorption edges are observed. The typical x-ray absorption spectrum for the nickel *K* edge in a NiO polycrystal is shown in Fig. 1. It exhibits an oscillating fine structure, which extends far from the absorption edge. For convenient interpretation, two regions are often separated: (i) the x-ray absorption near-edge structure (XANES), and (ii) the extended x-ray absorption fine structure (EXAFS).

It is agreed that the XANES region extends for 50-100 eV beyond an absorption edge and is determined by the local density of vacant states in an absorbing atom, as well as by multiple-scattering effects, i.e., scattering of an excited photoelectron on several atoms. The farther EXAFS region is dominated by the single scattering processes and extends up to 400-2000 eV from an edge. Its upper bound is determined by the signal-to-noise ratio and/or another absorption edge. Note that this division of an x-ray absorption spectrum into

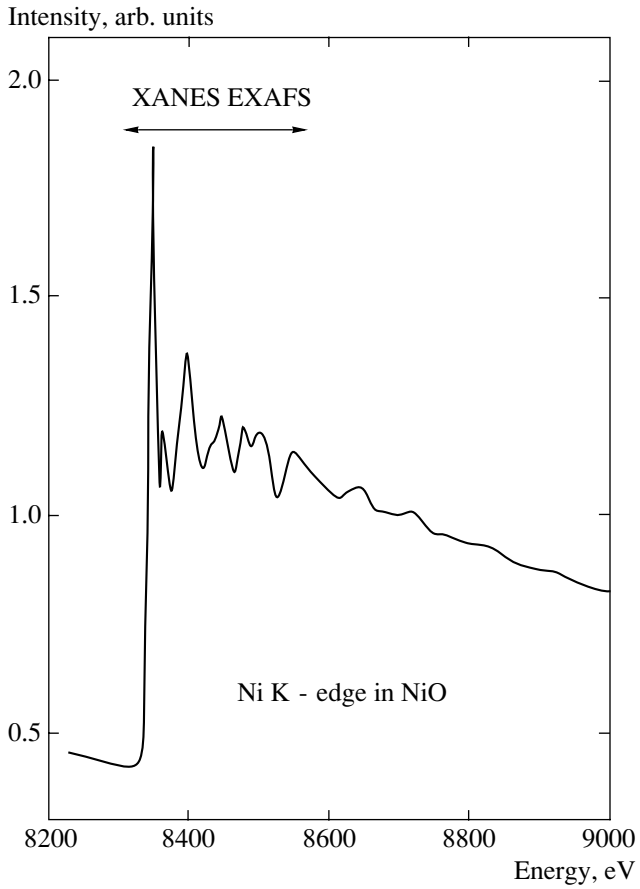

Fig. 1. The x-ray nickel *K* edge absorption spectrum from NiO [31].

two regions is conventional and the intervals of these regions can vary for various compounds. For this reason, the term x-ray absorption fine structure (XAFS) is now often used for the whole oscillating component beyond an absorption edge.

A fine structure beyond an absorption edge was first observed about 70 years ago [2-8]. However, it took more than 40 years to interpret this phenomenon. In 1931, Kronig [9] was the first who attempted to explain XAFS by the long-range order in a system. Later, this mechanism broke down. One year later, Kronig [10] proposed another theory, which was based on the substantial importance of short-range order and attributed XAFS to the modulation of the final-state wave function of a photoelectron scattered on the neighboring atoms. This approach was later further developed [11-15] and provides the basis of the current concept of the XAFS.

The fundamental development in x-ray absorption spectroscopy occurred in the early 1970s, when Sayers, Stern, and Lytle [16] demonstrated that the Fourier transform of the EXAFS oscillations gives a pattern close to the radial atomic density distribution. This circumstance testified to the crystallographic origin of information contained in the EXAFS oscillations. Moreover, the spectroscopic measurements in the XANES region with soft x-rays from 300 eV to 10 keV were shown to provide information on vacant states near the Fermi level with high energy resolution [17, 18]. The use of synchrotron radiation (SR) as a source of a continuous spectrum significantly stimulated the development of EXAFS spectroscopy and its various applications. The SR sources are many orders of magnitude brighter than x-ray tubes and ensure quick (as short as several milliseconds) EXAFS-spectrum measurement for low densities of an element [19].

The first SR sources were designed at the storage rings VEPP-3, Russia, in 1971; ADONE, Italy, 1979; ACO, France, 1970; and SPEAR, Stanford University, California, USA, 1973 [20]. At present, the third-generation SR sources ESRF, France; ALS and APS, USA; ELETTRA, Italy; and SPRING8, Japan with radiation brightness up to $\sim 10^{19}$ photons are in operation. More than 50 sources are now in operation and more than 10 are being designed [20]. Having high brightness and distinct linear or circular polarization, SR provides unique research possibilities. In particular, new XAS methods, which were developed for studying atomic and electronic structures in both the bulk and the surface layers of various thickness values, are as follows:

(i) fluorescent EXAFS (FEXAFS) spectroscopy;

(ii) surface EXAFS (SEXAFS) spectroscopy by measuring Auger electrons, the total or partial yield of the photoelectron current, the yield of the photoinduced ion desorption, and the total internal reflection;

(iii) EXAFS spectroscopy of x-ray excited optical luminescence (XEOL);

(iv) the method of measuring the circular magnetic x-ray dichroism (CMXD) applicable to the investigation of the magnetic properties of materials [21]; and

(v) EXAFS spectroscopy by measuring the intensities of Bragg peaks-diffraction anomalous fine structure (DAFS).

This paper reviews the experimental possibilities of EXAFS spectroscopy for the physics of condensed matter in view of the commissioning by JINR of the energy-dispersive spectrometer in the SR beam at Kurchatov Institute, as well as the designing of the specialized third-generation SR source DELSI at JINR. Since this review is intended for specialists in solid state physics, it does not include the biological aspect of XAS.

2. BASIC THEORETICAL PRINCIPLES OF X-RAY ABSORPTION SPECTROSCOPY. METHOD FOR ANALYZING EXAFS SPECTRA

X-ray absorption spectroscopy is based on the interaction of incident radiation with a solid. Figure 2 shows the basic elementary processes induced by the passage of radiation through a substance. The processes attenuate the intensity of x-rays traversing a sample as $I_x = I_0 \exp(-\mu x)$, where the absorption coefficient μ is determined by various elementary processes, such as photo-

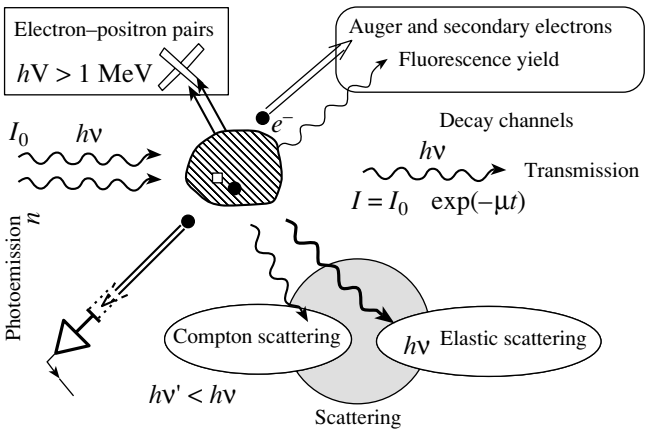

Fig. 2. The elementary processes of interaction of x-rays with a substance.

electron absorption, Compton scattering, elastic scattering, and pair production [22].

For photon energies ω below 100 keV, photoelectron absorption, which is accompanied by emission of a photoelectron of the energy $E = \hbar\omega - E_0$, where E_0 is the binding energy of electrons in an absorbing atom, has a maximal cross section. For incident photon energies 300–30000 eV, the photoelectron energy E is 1–1000 eV.

The absorption of an x-ray photon by an atom leads to excitation, which is relaxed either through emission of individual photons (fluorescence) or ejection of Auger electrons with definite energies corresponding to the levels of the atomic system. Figure 3 shows the diagram of relaxation of the exited atomic state. The probability of various decay channels (Auger process and fluorescence) depends on the charge of the nucleus and is shown in Fig. 4 as the charge dependence of the level width [23]. The level widths determine the experimental resolution necessary for their separation.

In the dipole approximation, the cross section σ for photon absorption by an atom is expressed in terms of the transition probability, i.e., $\sigma = 2\pi/\hbar \sum \langle f|\hat{W}|i\rangle^2 \delta(E_f - E_i - \omega)$, where the operator $\hat{W}$ of the dipole transition induced by incident electromagnetic radiation is represented as $\hat{W} = e\mathbf{r}\cdot\mathbf{E}$, where $\mathbf{E}$ is the electric field vector in the incident wave and $e\mathbf{r}$ is the atomic dipole moment [24], and E_f and E_i are the energies of the atom in the final and initial states, respectively.

In terms of the polarization vector $\boldsymbol{\varepsilon} = \mathbf{E}/|E|$, the absorption cross section for the dipole and quadrupole transitions has the form [24]

$$\sigma(\omega) = 4\pi\alpha^2\hbar\omega\sum\langle f|\boldsymbol{\varepsilon}\cdot\mathbf{r}|i\rangle\delta(E_f - E_i - \hbar\omega), \quad (1)$$

$$\sigma(\omega) = 4\pi\alpha^2\frac{1}{4}\hbar\omega\sum\langle f|(\boldsymbol{\varepsilon}\cdot\mathbf{r})(\mathbf{k}\cdot\mathbf{r})|i\rangle^2 \times\delta(E_f - E_i - \hbar\omega), \quad (2)$$

respectively.

These formulas indicate that the process has the following features:

(i) excitation selectivity governed by the photon energy ω;

(ii) dichroism determined by the dipole-transition operator $\boldsymbol{\varepsilon}\cdot\mathbf{r}$ with the components $\mathbf{e}\times\mathbf{z}$ or $(\varepsilon_x - i\varepsilon_y)(\varepsilon_x + i\varepsilon_y)$;

(iii) selection rules $\Delta l = \pm 1$; and

(iv) the effect of final-state relaxation on the total transition probability.

The energy dependence of the excitation cross section for neutral atoms, which do not interact with each other, is determined by the selection rule $\Delta l = \pm 1$ in the orbital angular momentum and the energy conservation law $\delta(E_f - E_i - \omega)$. Figure 5 shows the photoabsorption cross sections for neon atoms whose initial and final states are $|i\rangle = |1s^2 2s^2 2p^6\rangle$ and $|f\rangle = |1s'\ldots np^1\rangle$, respec-

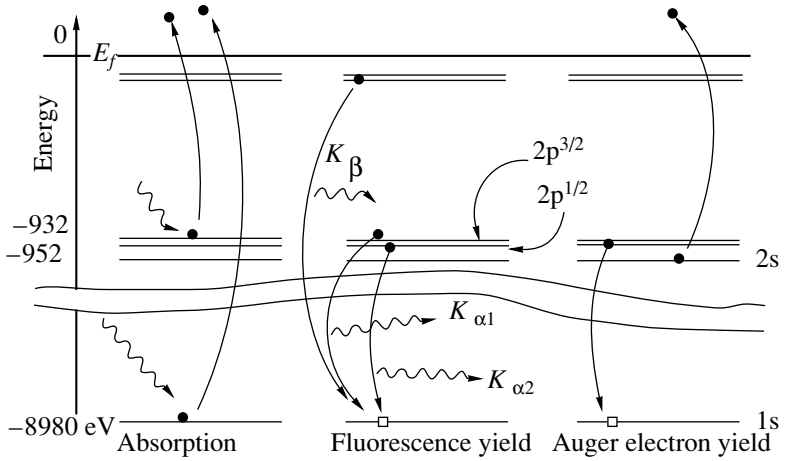

Fig. 3. Diagram of relaxation of an atomic state [25] exited by the absorbed x-ray photon.

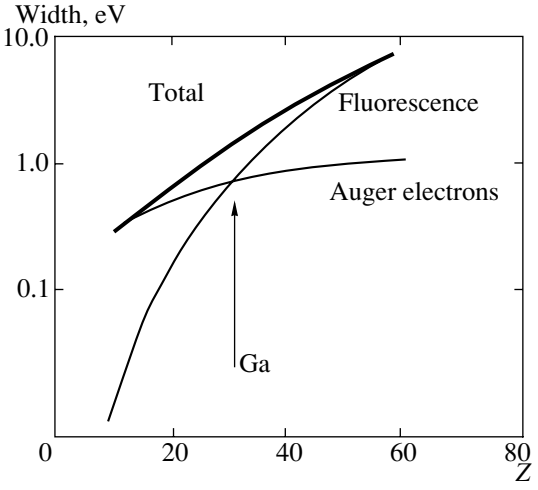

Fig. 4. The *K*-shell level width [25] as a function of the charge of a nucleus.

tively, as functions of the energy of an x-ray photon [25], and demonstrates that the photoabsorption cross section is completely determined by the energy levels of an individual atom.

The interaction pattern gets considerably more complicated when a photon is absorbed by an atom surrounded by neighboring atoms. Figure 6 illustrates the absorption of photons by an atom in a solid. At photon energies higher than the electron binding energy in the atom, an electron of the energy E and wave vector $\mathbf{k}$ is excited. This electron is scattered on the atoms of the nearest environment including the absorbing atom. For low photoelectron energies and correspondingly long de Broglie wavelengths commensurate with the interatomic distance R_0 in a crystal lattice, which corresponds to the XANES region, the multiple-scattering contribution usually far exceeds the single-scattering one. For high photoelectron energies, the de Broglie

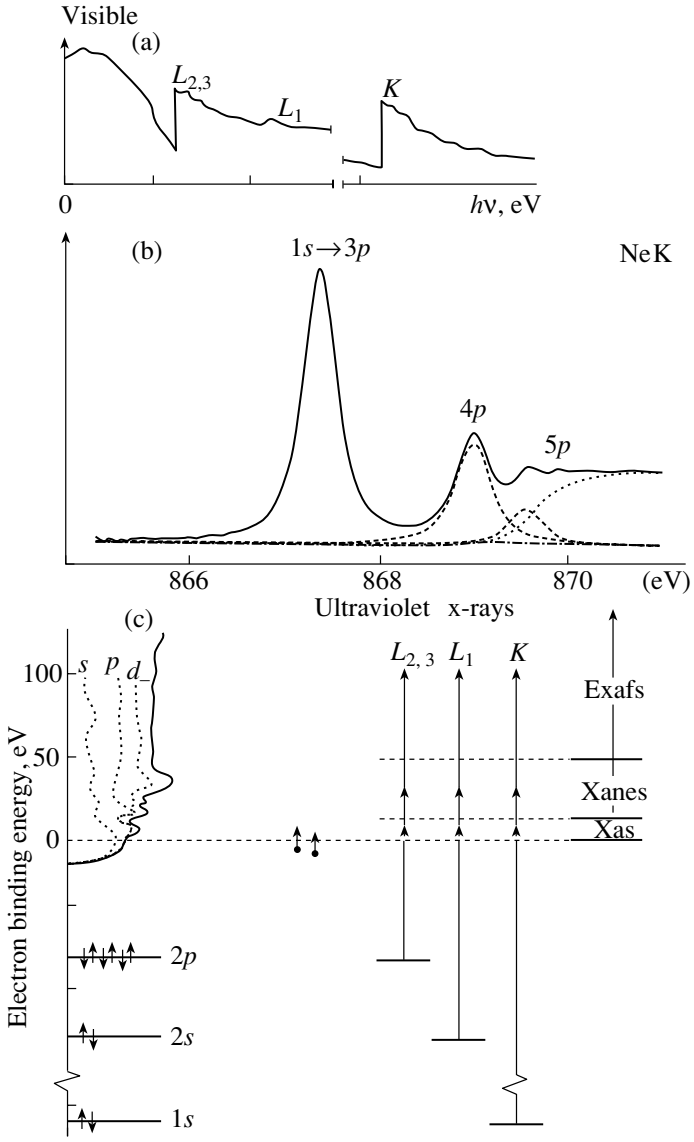

Fig. 5. The photoabsorption cross section σ for neon as a function of the energy of x-ray photons (a) in a wide energy range and (b) near the *K* edge and (c) diagram of the energy levels of neon.

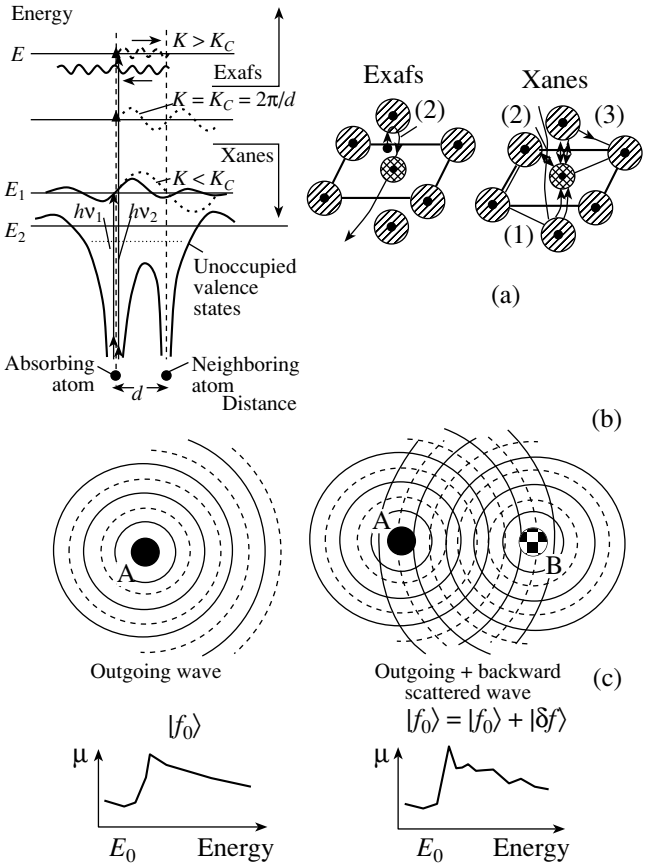

Fig. 6. (a) Diagram of electron energy levels in a crystal lattice for various excitation energies corresponding to the (EXAFS) single and (XANES) multiple scattering processes; (b) outgoing wave corresponding to a free electron and interference of outgoing scattered wave: (A) the atom absorbing an x-ray photon, (B) a neighboring atom; and (C) energy dependence of the x-ray absorption coefficient μ if the scattering by neighboring atoms is disregarded (left) and taken into account (right).

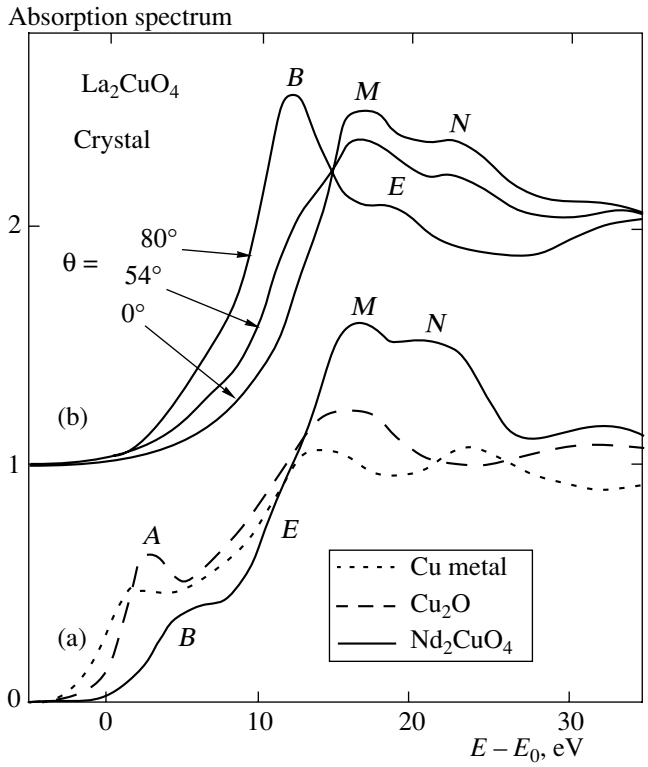

Fig. 7. The XANES spectra measured at various angles of x-ray incidence on the crystal surface plane [25].

wavelengths are very short and, therefore, single scattering dominates.

The XANES region includes information on the electronic state of the absorbing atom (valence and vacant-state density) [25, 26]. Figure 7 shows the XANES spectra measured at various angles for pure metals, powders, and single crystals [25]. The angular dependence of the spectra indicates that polarized synchrotron radiation efficiently interacts with various configuration electrons: photons that are incident on single crystals La_2CuO_4 at $\theta = 0°$ interact with the (*ab*)-plane electrons in the 4*px*, *y* orbitals. This corresponds to the peaks *M* and *N*. For $\theta \geq 54°$, the interaction with 4*pz*-orbital electrons occurs (*BE* transitions).

The EXAFS model serves to represent the transition probabilities from the initial atomic state to an excited final state, which is described by the wave function of a free electron emitted due to the absorption of an ω photon. The electron is scattered on an atom if such an atom is located near the absorbing atom. As a result, the initial and scattered waves arise and interfere with each other. The phase differences is determined by the interatomic distance and electron wave number *k*. Figure 6 shows the schemes of all processes accompanying the absorption of a photon whose energy $\hbar\omega$ is above the threshold E_0 of photoelectron ejection in the solid. As was mentioned above, the cross section for interaction between the photon and an atom is determined by Eq. (1) that takes the form

$$\sigma = |M|^2 \sum \int d^3x \left|\varphi_{\text{res}}(x)\boldsymbol{\varepsilon}\cdot\mathbf{r}\cdot\varphi_{i_f}\right|^2 \times \delta(E_i - E_{f,\text{R}} - \hbar\omega + \varepsilon_f), \quad (3)$$

where $M = \langle \Psi_i^{N-1} | \Psi_{f,\text{R}}^{N-1} \rangle$ is the matrix element of the monopole transition from the initial state of the $(N-1)$-electron system excluding the excited electron of the energy ε_f to the state of completely relaxing $N-1$ electrons.

The final state wave function of the electron moving in the potential of remaining $N-1$ electrons in the ground state is calculated with allowance for the interaction of this electron with neighboring atoms including vacancies formed in the core.

In the single scattering approximation, the wave function has the general form

$$\varphi_{\varepsilon_f}(x) = \varphi_\varepsilon^{\text{abs}}(x) + \sum_{R_j} \varphi_\varepsilon^{\text{scat}}(x - R_j), \quad (4)$$

where $\varphi_\varepsilon^{abs}$ is the wave function of the free electron emitted in photon absorption, and $\varphi_\varepsilon^{scat}(x - R_j)$ is the wave function of the electron scattered by an atom located at the distance R_j away from the atom absorbing the photon. Substituting Eq. (4) into Eq. (3), we obtain the cross section for interaction of the photon with the atom accounting for the nearest environment:

$$\sigma(\omega) = \sigma^{abs}(\omega)(1 + \chi(\omega)). \quad (5)$$

Here, $\sigma^{abs}(\omega)$ is the classical cross section for photon scattering and the EXAFS modulation $\chi(\omega)$ of the atomic cross section by the nearest environment is represented as

$$\chi(\omega) = \frac{1}{\sigma^{abs}(\omega)}\sum_{R_j} 2R_j \int d^3x \varphi^*_{ires}(x)\boldsymbol{\varepsilon}\cdot\mathbf{x}\cdot\varphi^{abs}_{\varepsilon, lm} \times \int d^3x' \varphi^*_{ires}(x')\boldsymbol{\varepsilon}\cdot\mathbf{x}\cdot\varphi^{scat}_{\varepsilon lm R_j}(x'), \quad (6)$$

where $\varphi^{abs}_{\varepsilon lm}$ is the wave function of the electron emitted with the energy ε and orbital angular momentum l from the atom, and $\varphi^{scat}_{\varepsilon lm R_j}$ is the wave scattered from the neighboring atom located at the point R_j. The quantum numbers of the outgoing wave are determined by the selection rule for the $l = 1$ dipole transition for the K and L absorption.

In the EXAFS region, where the photoelectron wave number k_e is higher than the wave number $k_d = \frac{2\pi}{d}$ corresponding to the first Brillouin zone (see Fig. 6), the scattered wave function at the distance $|x - R_j|$ from the scattering atom can be represented in the asymptotic form

$$\varphi^{scat}_{\varepsilon lm}(x) = \varphi^{abs}_{\varepsilon lm}(R_j) f(\Omega_k) e^{i|k|x} e^{-\mu(|R_j| + |x|)} \frac{1}{|x|} = Y_{lm}(\Omega_{R_j}) e^{i(kR_j + \delta_1)} f(\Omega_k) e^{i|k|x} e^{-\mu(|R_j| + |x|)} \frac{1}{|k|R_j|x|}, \quad (7)$$

where δ_1 is the phase shift of the wave in the absorbing atom, Ω_k is the scattering solid angle with respect to the scattering atom, $\Omega_{R_j}(\theta, \varphi)$ is the solid angle with respect to the straight line connecting the absorbing and scattering atoms, and $f(\Omega_k)$ is the scattering length for the angle Ω_k.

Calculation of the matrix element $\chi(\omega)$ for the distribution versus $\{R_j\}$ yields

$$\chi(\omega(\{R_j\})) = \sum_j \frac{|\boldsymbol{\varepsilon}\mathbf{R}_j|}{k|R_j|^2} \mathrm{Im}\{f(\pi) e^{2ik|R_j|} e^{2i\delta_e}\} e^{-2\mu R_j}, \quad (8)$$

where $f(\pi) = \sum_{l'} \frac{e^{2i\delta_{e'}} - 1}{2ik}(2l' + 1)(-1)^{l'}$ is the backward scattering amplitude and the exponential $e^{-\mu(|R_j| + |x|)}$ determines the electron mean free path in the substance.

Because environment atoms undergo thermal vibrations in a solid, the expression for $\chi(\omega; \{R_j\})$ should be averaged over the distribution $g(R_j)$ of the vibration amplitudes:

$$\bar{\chi}(\omega) = \sum_j \int d^3R_j g(R_j)\chi(\omega; \{R_j\}). \quad (9)$$

For a simple crystal, this averaging depends on the relative direction between the incident-wave polarization vector $\boldsymbol{\varepsilon}$ and the crystallographic axis. For a polycrystal sample, averaging is performed over all directions and only variations in magnitude of $|R|$ are of importance.

The simplest approximation in $\{R_j\}$ is the Gaussian dependence with the variance σ^2. The EXAFS factor $\chi(\omega)$ is expressed in terms of the mean quantities as

$$\bar{\chi}(\omega) = \sum_j \frac{f(\pi)}{k|\bar{R}_j|^2} \sin(2|k|R_j + \bar{\alpha}(k)) e^{-k^2\sigma^2} e^{-2\mu R_j}, \quad (10)$$

where the phase shift $\alpha(k)$ depends on temperature and has the form

$$\alpha_j(\bar{k}) = \left(2\delta_e + \arg f(\pi) - \frac{2k\sigma^2}{R_j} - 2k\mu\sigma^2\right). \quad (11)$$

The Debye-Waller factor $e^{-k^2\sigma^2}$ in Eq. (10) reflects the contribution of the rms deviation of the interatomic distance from the mean value in thermal vibrations. It should be emphasized that the parameter σ differs from the rms atomic deviation, which is used in the correction of the Bragg scattering: the latter determines the displacement of an atom from its equilibrium position, whereas the parameter σ in the EXAFS spectroscopy specifies variation in the absorber-scatterer distance R_j.

The phase shift δ_e, which is determined by the central atom, is a function of the Coulomb atomic potential defined by the effective charge Z_{eff} of an ion [24] as $\delta_e = \delta_e^0 + Z_{eff}^2 \log(R_j/a_B)/(a_B k)$, where a_B is the Bohr radius.

Taking into account that the local environment atoms are described by the pair correlation function $g_j(r)$, where r is the distance between the absorbing and probe atoms, we can represent the EXAFS formula in the form

$$\chi(k) = \sum_j \frac{f_j(\pi k)}{k} \times \int_0^\infty dr g_j(r) \sin(2kr_j + \alpha_j(k)) e^{-k^2\sigma^2} e^{-2\mu(k)r_j}. \quad (12)$$

Two basic factors strongly depending on the state under investigation have to be taken into account each time Eq. (12) is applied: (i) errors caused by neglecting multiple scattering of an excited electron on atoms and (ii) the coordination-disorder degree determined by the origin of the distribution $g_j(r)$.

For discrete distribution of the scattering atoms in the number N_j of atoms in the jth coordination sphere and in the distance R_j to the jth coordination sphere, the EXAFS distribution function $\chi(k)$ has the form

$$\chi(k) = \sum A_j(k) \sin(2kR_j + \bar{\alpha}_j(k)),$$
$$A_j(k) = \frac{N_j}{kR_j^2} F_j(k) e^{-2k^2\sigma^2}. \quad (13)$$

Here, $F_j(k) = f(k)e^{-2R_j/\lambda}$, where λ is the mean free path of electrons, and the scattering phase shift is represented as

$$\bar{\alpha}_j(k) = 2kR_j + \delta_j(k) + \Theta_j(k),$$

where $\delta_j(k)$ is the phase shift determined by the scattering atom, θ_j is the phase shift related to the complex part of the backward scattering amplitude $f_j(k, \pi) = |f_j(k, \pi)|\exp\{i\theta_j(k)\}$ of electrons. Figure 8 shows the quantities δ_j and θ_j calculated according to [27]. The backward scattering amplitude $f(k)$ is similarly calculated on the basis of the results obtained in [27].

The energy dependence of the mean free path λ of a photoelectron with the energy E is given as $\lambda = \frac{\pi}{\Gamma_h(E)}\left(\frac{2E}{m}\right)^{1/2}$, where Γ_h is the hole-level width. This quantity determines the effective number of the coordination spheres that are seen in the EXAFS process and is shown in Fig. 9 [28].

We now discuss the behavior of the backward scattering amplitude $f(k, \pi)$. In the modulation part $\chi(\omega)$ of the absorption amplitude, the component of the backward scattering of a photoelectron by the nearest atom depends on its Coulomb potential $V_{scat} f(\pi, k) = \int d^3 r V_{scat}(r) e^{ikr}$. Using the shielded Coulomb potential $V_{scat}(r) = Z_{eff} e^2 \frac{e^{-\mu r}}{r}$, we obtain the scattering amplitude in the form $f(\pi, k) = \frac{4\pi e^2 Z_{eff}}{(\mu^2 + k^2)}$.

Figure 10 shows the theoretical dependence of the backward scattering amplitude for various elements

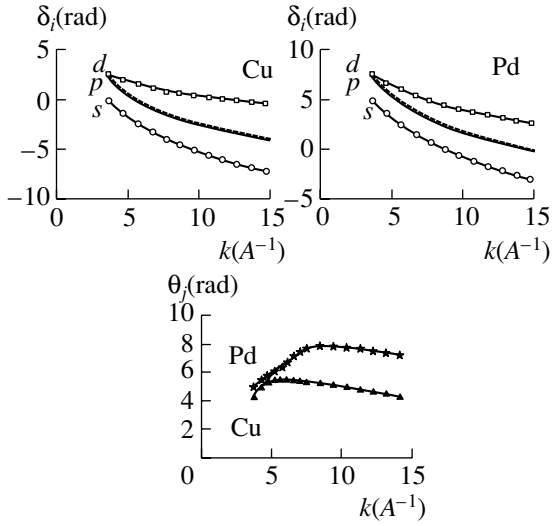

Fig. 8. The phase shifts (a) δ_i and (b) θ_j as a function of the wave number k [41].

and demonstrates that $f(\pi, k)$ rapidly decreases with the electron momentum for small-Z atoms and has a large value for large-Z atoms. This difference in the scattering amplitudes can be used to separate various contributions to the EXAFS spectra.

Thus, we have analyzed the formation of the fine structure originating in the x-ray absorption spectrum from interfering with the electron wave scattered from the absorbing atom and electron waves scattered on the nearest environment atoms. This interpretation distinctly corroborates the local sensitivity of the method and its applicability for both crystalline and disordered substances.

The Fourier transform of the EXAFS function $\chi(k)$ makes it possible to determine the density quasidistribution $F(R)$ in the coordinate space as $F(R) = \frac{1}{2\pi}\int_{k_{min}}^{k_{max}} W(k)\chi(k)e^{2ikR}dk$, where k_{min} and k_{max} are the minimum and maximum values of the photoelectron momentum $k = \sqrt{\frac{2m}{h^2}(E - E_0)}$, where E is the incident photon energy, and E_0 is the threshold of photoelectron emission from the corresponding absorbing-atom level. The window function $W(k)$ [$W(k) \longrightarrow 0$ at $k \longrightarrow \pm\infty$] is used to extend the limits of integration to $k \longrightarrow \pm\infty$, which is necessary to correctly calculate the Fourier transform.

We now discuss the Debye-Waller factor σ, which, for EXAFS spectroscopy, governs the variance of the distance between the absorbing and scattering atoms $\sigma^2 = \langle|\mathbf{R}_{ab}|\mathbf{u}_b - \mathbf{u}_a|\rangle$, where $\mathbf{R}_{ab}$ is the vector connecting the atoms a and b and $\mathbf{u}_a$, and $\mathbf{u}_b$ are the vectors of deviation of the positions of respective atoms a and b from the crystal center. From this expression, we obtain $\sigma^2 =$

Table 1. Parameters of crystals at room temperature [30]

Z	Atomic mass *M*	Crystal	Structure	Debye temperature θ, K	$u_x^{1/2}$, Å	Lattice constant, Å
6	12.01	C	fcc (diamond)	2000	0.04	3.567
13	26.96	Al	fcc	390	0.105	4.050
14	28.09	Si	fcc	543	0.075	5.431
23	50.94	V	bcc	360	0.082	3.024
24	52	Cr	bcc	485	0.061	2.884
26	55.85	Fe	bcc	420	0.068	2.867
29	63.54	Cu	fcc	315	0.084	3.615
32	72.59	Ge	fcc (diamond)	290	0.085	5.657
41	92.91	Ne	bcc	275	0.079	3.300
47	107.87	Ag	fcc	215	0.093	4.086
74	183.85	W	bcc	310	0.050	3.116
79	196.97	Au	fcc	170	0.087	4.078
82	207.19	Pb	fcc	88	0.16	4.951

$2u_x^2 - 2DCF$, where the deviation correlation function $DCF = \langle \mathbf{u}_a \cdot \mathbf{u}_b \rangle$ is determined by the structural features of the object and can be found in [29]. The rms deviation u_x is expressed in terms of the temperature T as [24]

$$u_x^2 = \frac{3h^2}{k_B M\Theta}\left\{\frac{\Phi(\Theta/T)}{\Theta/T} + \frac{1}{4}\right\},$$

where h and k_B are the Planck and Boltzmann constants, respectively; M is the atomic mass, Θ is the Debye temperature, and the Debye function has the form

$$\Phi(x) = \frac{1}{4}\int_0^x \frac{y\,dy}{\exp\{y\} - 1}.$$

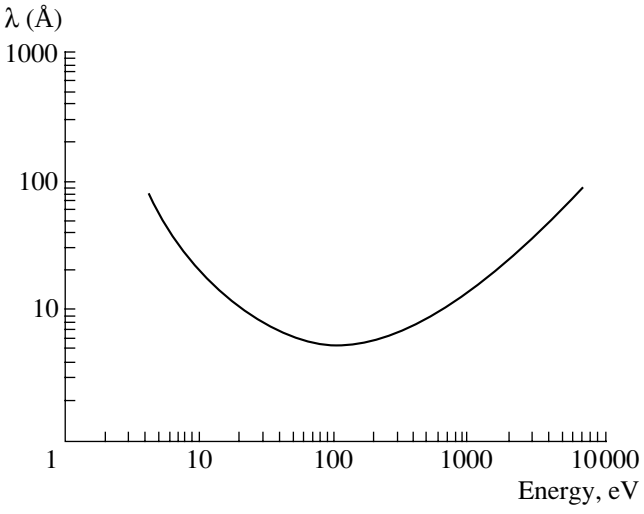

Fig. 9. Universal curve describing energy dependence of the mean free path λ of photoelectrons [28].

Substituting the values of the constants into the above formula for the function u_x^2 (Å²), we obtain $u_x^2 = \frac{439}{M\Theta}\left\{\frac{\Phi(x)}{x} + \frac{1}{4}\right\}$ (Å²).

Table 1 presents the parameters of crystals at room temperature [30].

Thermal vibrations are responsible for the temperature dependence of the diffracted radiation. The intensity of diffraction maxima decreases with increasing temperature as $I = I_0\exp\{-2D\}$. For x-ray diffraction, $D = \frac{1}{3}\frac{u_x^2}{\Delta k^2}$, where $\Delta k = 2\pi/\lambda\sin\theta$ is the value of the momentum transfer in x-ray quantum scattering.

Figure 11 shows the EXAFS functions $\chi(k)$ measured for various temperatures at the rhenium L_3 edge in the ReO_3 polycrystal [31, 32]. Figure 12 shows their Fourier transforms $F(r)$, which exhibit peaks corresponding to the coordination spheres around the central rhenium atom. It should be noted that the position and shape of the peaks of the function $F(r)$ are always distorted because of the presence of the phase shift $\alpha(k)$ and the amplitude modulation $f(k)$, which is the fundamental difference between the Fourier transform $F(r)$ of the EXAFS function and the actual pair correlation function $g(r)$ [see Eq. (12)].

2.1. Method for Analyzing EXAFS Spectra

As was mentioned above in Section 2, information on the local structure is carried by the EXAFS, which has oscillating behavior and is extended beyond an atomic absorption edge. The EXAFS oscillations are usually observed in the 400–2000 eV range above an

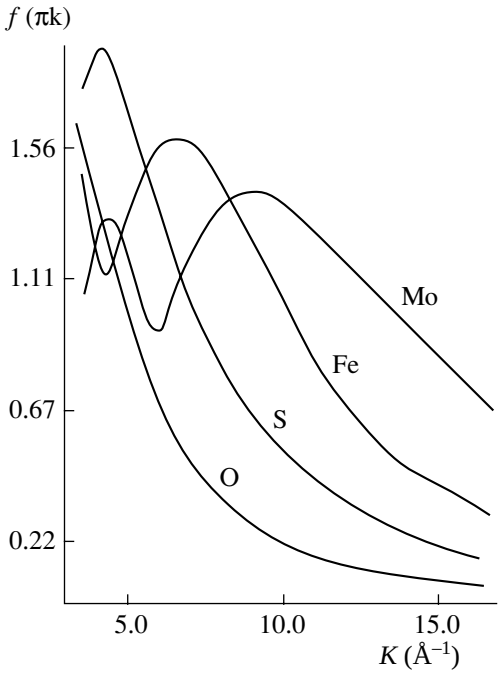

Fig. 10. Backward electron scattering amplitude as a function of the wave number k for various elements [24].

absorption edge, and this range is restricted by the noise pollution of the experimental signal and/or the presence of another absorption edge. Being developed in the last two decades, the general approach [33–35] to an analysis of EXAFS spectra implies the intensive use of modern computers for fast calculations and graphic representation of the results in the interactive regime. Below, we will briefly describe the method for processing of EXAFS spectra by using the EDA (EXAFS Data Analysis) software package, which was developed by one of us (A.Y.K.) at the Institute of Solid State Physics, University of Latvia, Riga, Latvia in 1988-1998 [36-38].

The EDA package is written for IBM PC compatible computers with MS DOS and, in the 5.1 version, consists of eight interactive codes (EDAFORM, EDAXANES, EDAEES, EDAFIT, EDARDF, FTEST, and EDAPLOT), which completely realize both the standard procedure of the processing and calculation of EXAFS spectra [33-35] and some original approaches used for selecting and simulating the EXAFS component [36-38]. The package has an open architecture and, therefore, can easily be extended. The procedure of the analysis of the EXAFS spectra realized in the EDA package is shown schematically in Fig. 13.

The EDAFORM code calculates the x-ray absorption coefficient $\mu(E)$ from measured x-ray intensities before, $I_0(E)$, and after, $I(E)$, interaction with a sample. According to the most extensively used transmission measurement procedure, these intensities correspond to the intensities of the radiations incident on the sample and passing through it, respectively, and the absorption coefficient of the sample with the thickness x is determined as $\mu(E) = (1/x)\ln[I_0(E)/I(E)]$.

The shape of the coefficient of x-ray absorption near the edge structure (XANES) is often of practical interest. This part of the spectrum is primarily determined by the local electronic structure, and its analysis remains a difficult problem. It requires, e.g., application of the theory of full multiple scattering (FMS) and quantum chemical cluster or band calculations [34, 35, 39], which are beyond the scope of this review. The EDA package cannot simulate the XANES, but the EDAXANES code enables one to separate the absorption coefficient $\mu(E)$

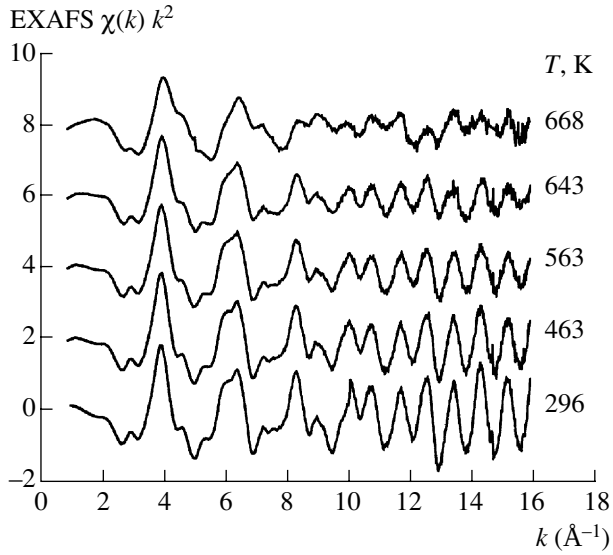

Fig. 11. The EXAFS spectra $\chi(k)k^2$ as a function of the wave number k for various temperatures near the rhenium L_3 absorption edge in ReO_3 [32].

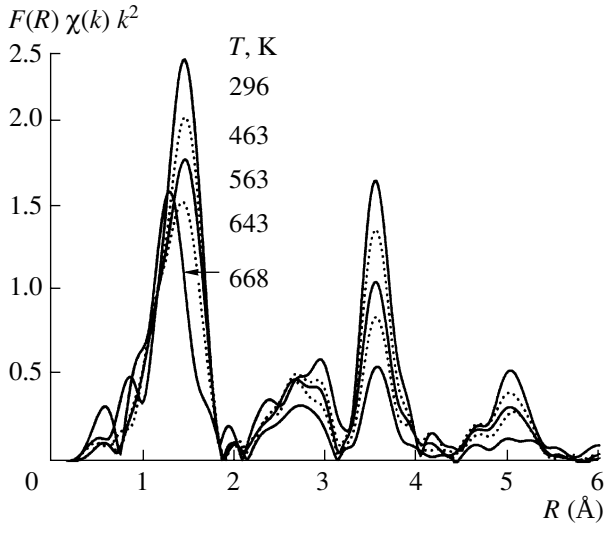

Fig. 12. The Fourier transforms $F(R)$ of the EXAFS spectra $\chi(k)k^2$ as a function of the distance R for various temperatures at the rhenium L_3 edge in ReO_3 [32].

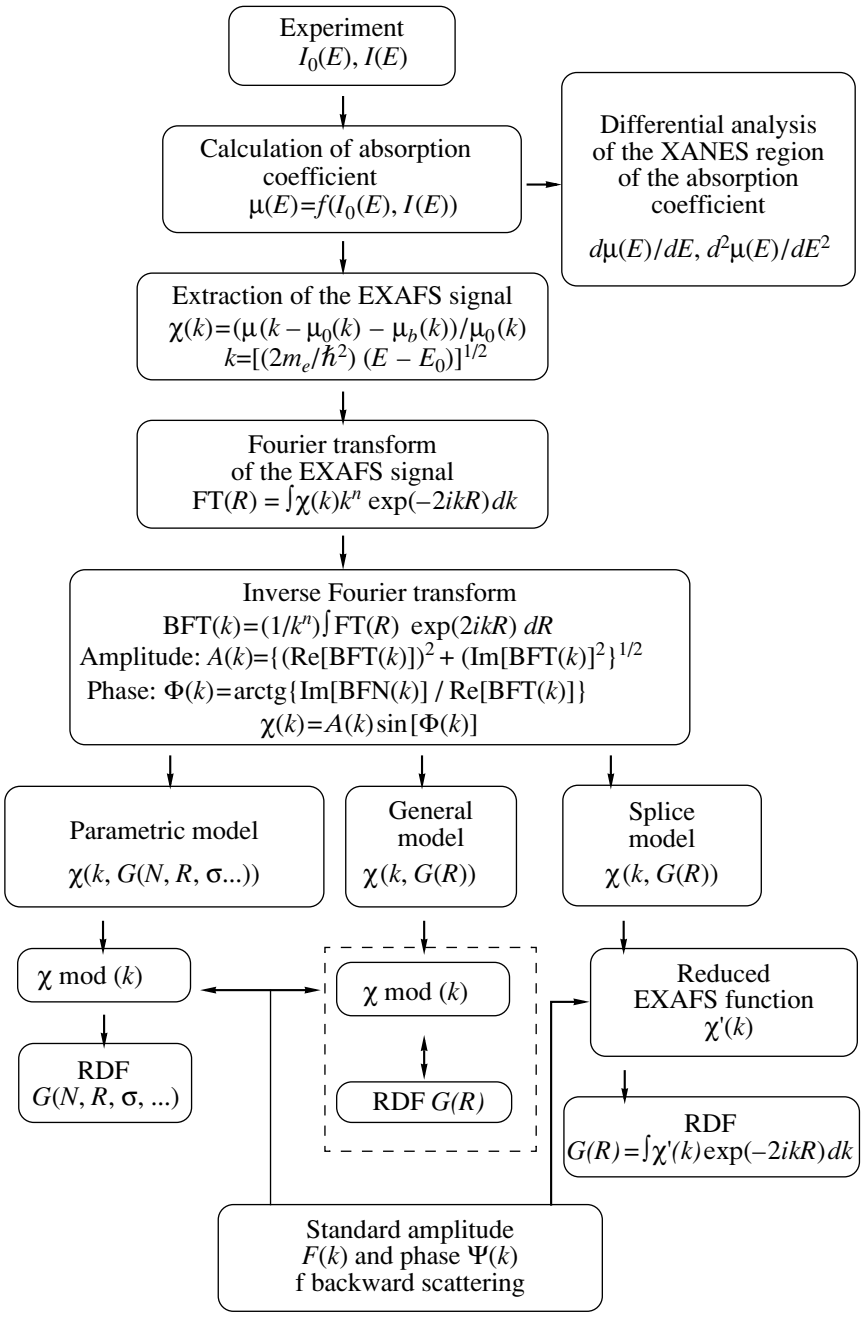

Fig. 13. Diagram of the EXAFS spectra analysis realized in the EDA software package [36-38].

near the edge structure and to analyze it differentially, e.g., to calculate the first, $d\mu(E)/dE$, and the second, $d^2\mu(E)/dE^2$, derivatives. This procedure considerably simplifies the qualitative analysis of the XANES and determination of the exact absorption-edge position, which is often used as the origin of the photoelectron kinetic energy in EXAFS spectra [33-35].

At the next stage of the x-ray absorption spectrum analysis, we isolate the EXAFS component $\chi(k)$, which is determined as [33–35]

$$\chi(k) = (\mu(k) - \mu_0(k) - \mu_b(k))/\mu_0(k),$$

where $\mu_b(k)$ is the absorption coefficient related to all processes excluding the photoionization of the atomic shell under investigation; $\mu_0(k)$ is the absorption coefficient for the case of the absence of atoms surrounding the absorbing one; $k = [(2m_e/\hbar^2)(\omega - E_0)]^{1/2}$ is the photoelectron wave number, where m_e is the electron mass; $\hbar$ is Planck's constant; E is the energy of incident photons; and E_0 is the ionization potential of the photon absorption.

At present, there are several software packages, EXCURE [40, 41], FEFF [42-45], and GNXAS [46-49], for *ab initio* simulation of the absorption spectrum without separation of the EXAFS signal. However, in many practical cases; e.g., when preliminary information on the compound structure is entirely or partially absent or the experimental signal is distorted, the application of the above-listed packages is strongly hampered. For this reason, the procedures of the isolation and analysis of the EXAFS component in most studies are separated, which considerably simplifies the problem. In the EDA package, the EDAEES code separates the EXAFS signal $\chi(k)$ by the original method [36, 38], whose advantage is in determining $\mu_0(k)$ by means of the procedure described below. The criterion of the correctness of $\mu_0(k)$ determination is the absence of any contribution besides the structural-origin oscillations in the EXAFS signal $\chi(k)$. For this reason, $\mu_0(k)$ is sometimes referred to as "zero line" of the EXAFS signal, i.e., the line around which the oscillating fine structure lies. Note that errors in $\mu_0(k)$ determination can result in substantial distortions in the EXAFS signal from the atoms of the first coordination sphere and, therefore, in the structure parameter values.

The absorption coefficient $\mu_b(E)$ is first approximated by the modified Viktorin polynomial $\mu_b(E) = A + B/E^3$, whose parameters A and B are determined by least squares fitting to the pre-edge part of the experimental absorption coefficient $\mu(E)$. Then, $\mu_b(E)$ is extrapolated to the entire range and is subtracted from $\mu(E)$ (see Fig. 14). The resulting function $\mu_1(E) = \mu(E) - \mu_b(E)$ is used at the first stage of determining μ_0, which is approximated by the polynomial $\mu_0^{\mathrm{I}}(E)$ of degree m_1, which is usually taken from 1 to 4, and is subtracted from the function $\mu_1(E)$ (see Fig. 14). The new function $\mu^{\mathrm{I}}(E) = \mu_1(E) - \mu_0^{\mathrm{I}}(E)$ is transformed to the k space and is multiplied by the factor k^n, where the power n is chosen to be equal to or larger than the value that will be used in further Fourier analysis and/or simulation; usually, $n = 1$, 2, or 3. At the second stage, we search for the function $\mu_0^{\mathrm{II}}(k)$ that is specified by the polynomial of degree m_2, which is usually taken from 0 to 9, and is the zero line for $\mu^{\mathrm{I}}(k)$. This operation corrects crude errors that are introduced to the behavior of the function $\mu^{\mathrm{I}}(E)$ when it is transformed to k space and multiplied by the factor k^n. Thus, at the first two stages, we obtain the function $\mu^{\mathrm{II}}(k) = \mu^{\mathrm{I}}(k) - \mu_0^{\mathrm{II}}(k)$ that is well oscillating around zero. At the third stage, we find the zero line $\mu_0^{\mathrm{III}}(k)$ of the function $\mu^{\mathrm{II}}(k)$ by cubic smoothing spline (see Fig. 15). It compensates for all remaining inaccuracies in the zero line. As a result, the desired function μ_0 is the sum of μ_0^{I}, μ_0^{II}, and μ_0^{III}. Figure 15b demonstrates the effect of the μ_0^{II} and μ_0^{III} corrections on the EXAFS signal.

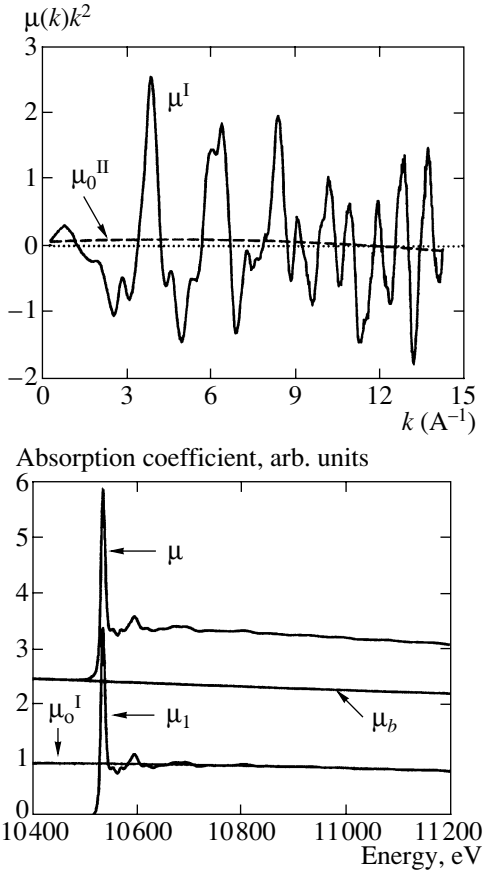

Fig. 14. (a) The function $\mu^{\mathrm{I}} = \mu_1 - \mu_0^{\mathrm{I}}$ transformed to the k space and multiplied by the wave number k^n, $n = 1$, and the second correction μ_0^{II} to μ_0 and (b) the experimental x-ray rhenium L_3 absorption spectrum in ReO_3 (μ) before and (μ_1) after the subtraction of the μ_b contribution and the first approximation μ_0^{I} to μ_0.

This effect is most pronounced in the Fourier transforms of the EXAFS signals (see Fig. 16); inaccuracies in the determination of the function μ_0 lead to the peak in the short-distance region $R < 1$ Å, which can distort the signal from the first coordination sphere (the principal peak near 1.4 Å).

In the most practical cases, the separated EXAFS signal is subjected to Fourier filtration, i.e., to direct and inverse Fourier transforms in the specified k and R ranges, to separate the contributions of individual coordination spheres, which considerably simplifies the signal simulation. In the EDA package, the Fourier filtration is implemented in the EDAFT code [38]. To perform the Fourier transform without introducing distortion to the EXAFS signal, because of its boundedness in the k space, the sharp shape of the EXAFS oscillations at the lowest and highest values of the wave number k is smoothed by the window function $W(k)$. In practice, the window function $W(k)$ is taken in the fol-

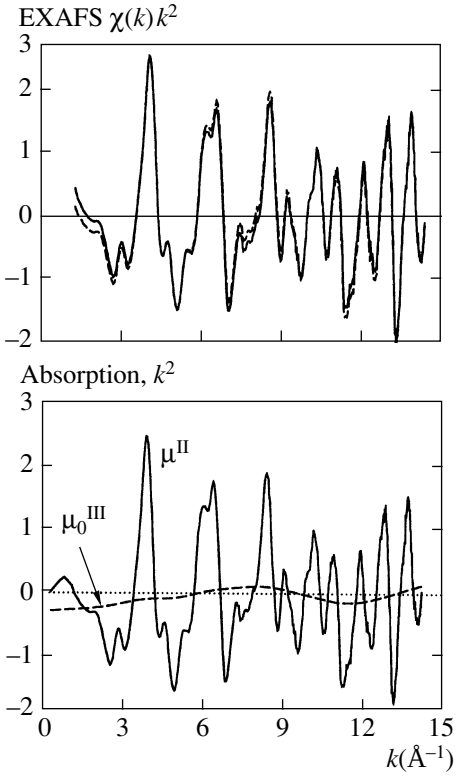

Fig. 15. (a) The function $\mu^{II} = \mu^{I} - \mu_0^{II}$ and the third correction μ_0^{III} obtained to μ_0 by cubic smoothing spline, and (b) the solid and dashed lines are the EXAFS signals calculated by the formulas $\chi(k) = [\mu(k) - \mu_0(k) - \mu_b(k)]/\mu_0(k)$ and $\chi(k) = [\mu(k) - \mu_0^{I}(k) - \mu_b(k)]/\mu_0^{I}(k)$, respectively.

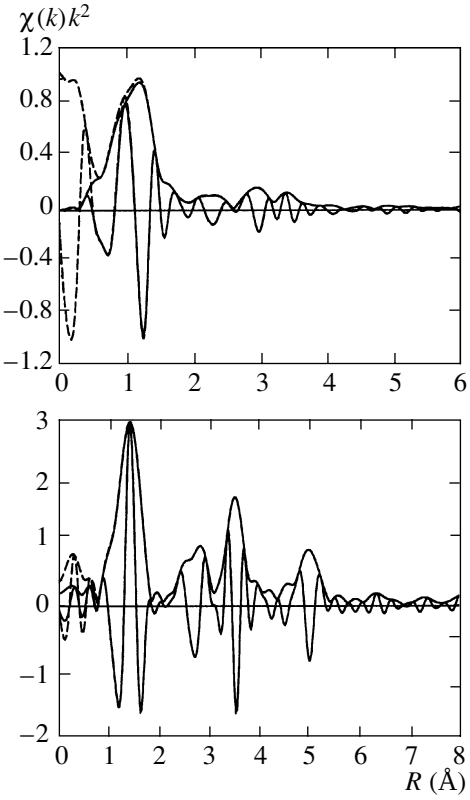

Fig. 16. The Fourier transforms $F(R)$ of the EXAFS signals $\chi(k)k^2$ from the (a) rhenium L_3 edge in ReO_3 and (b) molybdenum K edge in MoO_3 amorphous film. The EXAFS signals (solid line) $\mu_0 = \mu_0^{I} + \mu_0^{II} + \mu_0^{III}$ and (dashed line) $\mu_0 = \mu_0^{I}$ were extracted by the three-stage method described in the main body of the text and by the standard method, respectively.

lowing forms: rectangular, Hamming, Gaussian, Kayser-Bessel, etc. [33-35, 38]. Experience shows that the Gaussian and Kayser-Bessel window functions introduce the least distortion to the Fourier-transform procedure [38]. Note that, in the inverse Fourier transform, in addition to the EXAFS component $\chi(k)$, its total amplitude $A(k)$ and phase $\Phi(k)$ are calculated (see Fig. 13). These quantities can be used for evaluation of the amplitude $F(k)$ and phase $\Psi(k)$ of backward scattering with known structure parameters or for determining the relative change in the latter quantities by the method of comparison of the phases and amplitude ratio [33-35].

The Fourier transform of the EXAFS signal (see Fig. 16) is sometimes incorrectly treated, because it resembles the pair radial distribution function (RDF) of atoms. The Fourier transform fundamentally differs from the pair RDF because, first, the Fourier transform carries information on both the pair and multiatomic distribution functions [47, 48, 50, 51], second, the peak position does not correspond to the actual interatomic distances owing to the phase shift $\Psi(k)$ related to the backward scattering of a photoelectron on atoms [33-35], and third, the peak shape is distorted because of the contribution from the nonlinear backward-scattering amplitude $F(k)$ [33-35]. Moreover, each peak does not necessarily correspond to the specific group of atoms. In particular, the complex form of the amplitude and phase shift of the backward scattering on heavy elements results in two-hump peaks in the Fourier transform, where the hump heights depend strongly on the Fourier-transform interval [50]. Thus, the Fourier transform can provide only a rough measure of the distribution of atoms surrounding the absorbing center, and this distribution can be comprehensively interpreted only by simulation [50, 52-55].

At present, the structure parameters are determined from the EXAFS component $\chi(k)$, which is selected by Fourier filtering, by means of a number of approaches, whose success depends on the applicability of the approximations used in the simulation. The methods discussed below are implemented in the EDA package [36-38] and are intended to analyze the EXAFS signals from the first coordination sphere. Their applicability to analysis of remote coordination spheres is restricted by the multiple scattering effects (MSEs) determined by

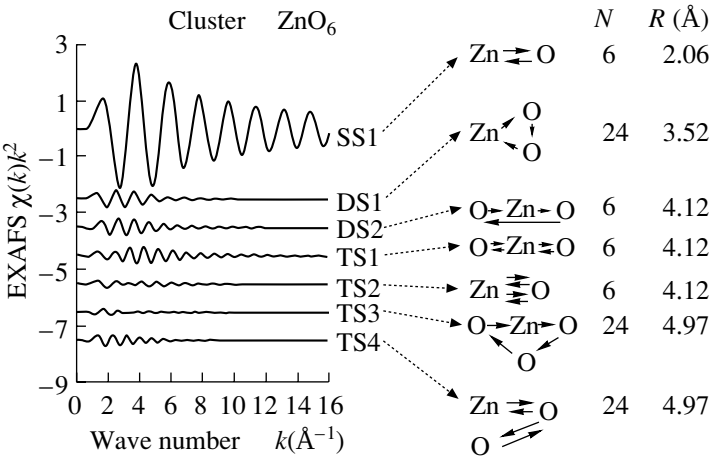

Fig. 17. Calculation of multiple scattering effects for the octahedral cluster ZnO_6; N is the number of identical scattering paths, R is the half-length of the path, and k is the wave number.

the contributions from the multiatomic distribution functions.

It is well known [50-52] that MSEs are always present beyond the first structural peak in the Fourier transform. The basic contribution in strongly disordered systems originates from the MSEs in the first coordination sphere, whereas the MSEs in the second and next spheres can additionally be manifested in ordered systems. Prominent examples of systems exhibiting MSEs are the compounds ReO_3, Na_xWO_3, and FeF_3 with a perovskite structure and aqueous solutions of some transition elements [50–52, 55–59]. The feature of these systems is the presence of linear, or close to linear atomic chains, which enhance the MSEs because of the so-called focusing effect. This effect is related to anisotropy in the atomic scattering amplitude and considerably increases the amplitude of the forward photoelectron scattering and, respectively, the EXAFS oscillation amplitude [50, 56].

The *ab initio* calculations of the EXAFS near the rhenium L_I and L_{III} edges in ReO_3 by the multiple scattering method [50, 52] demonstrated that the contributions from the multiple scattering in the linear chains O–Re_0–O and Re_0–O–Re (the subscript 0 corresponds to the absorbing atom) are quite considerable and are substantially responsible for the heights of the 2.5- and 3.5-Å peaks in the Fourier transform (see Fig. 16). It was also found that the large amplitude of the EXAFS signal above the L_{II} edge and the closeness between the L_{II} and L_I edges [$E(\mathrm{Re}L_I) - E(\mathrm{Re}L_{II}) = 568$ eV] lead to overlapping between the L_I and L_{II} EXAFS oscillations above the L_{II} edge. A similar pattern was observed in some tungsten oxides [56, 58]. The analysis of the EXAFS spectrum from the iron K edge in FeF_3, which has the rhombohedral distorted ReO_3-type structure revealed a contribution that comes from remote iron atoms spaced at 7.5 Å from the absorbing atom and is visible due to the MSEs [57, 58]. In this case, multiple scattering occurs in the Fe_0–F–Fe–F–Fe chain and the effect is called superfocusing [56].

In disordered systems (glasses [60], amorphous films [61-63], and solutions [55]), the MSEs in the first coordination sphere dominate. For octahedral coordination of the absorbing atom, as well as in the above-considered case, the basic contribution originates from the signals of multiple scattering in the almost linear atomic chains O–W_0–O [31, 32], O–Mo_0–O [31, 32], O–Ir_0–O [31, 32], and O–Zn_0–O [55]. The MSE contribution from remote coordination spheres is suppressed owing to the structural and dynamical disorder. Figure 17 shows an example of the calculation of the MSEs for the octahedral cluster ZnO_6 and demonstrates that, besides the single scattering signal *SS*1, noticeable contribution comes from the signals of double (*DS*1 and *DS*2) and triple (*TS*1 and *TS*4) scattering processes, which are responsible for the peaks in the Fourier transform of the EXAFS signal near the zinc K edge in the aqueous solution [55].

Thus, the possible presence of the multiple scattering contributions in the region of remote coordination spheres significantly complicates analysis of their EXAFS signals. Therefore, the correct application of the methods described below requires careful estimation of possible errors introduced by neglecting the MSEs.

In the most cases, the EXAFS signal from the first coordination sphere of the absorbing atom can be attributed to the mechanism of the single scattering of spherical waves [33-35]. Although this model is simple, an unambiguous analysis procedure for acquiring reliable structural information on the RDF of the first coordination sphere in an arbitrary compound does not exist.

At present, the following approaches are extensively used to analyze EXAFS signals: (i) the model dependent technique based on the parametrization of the

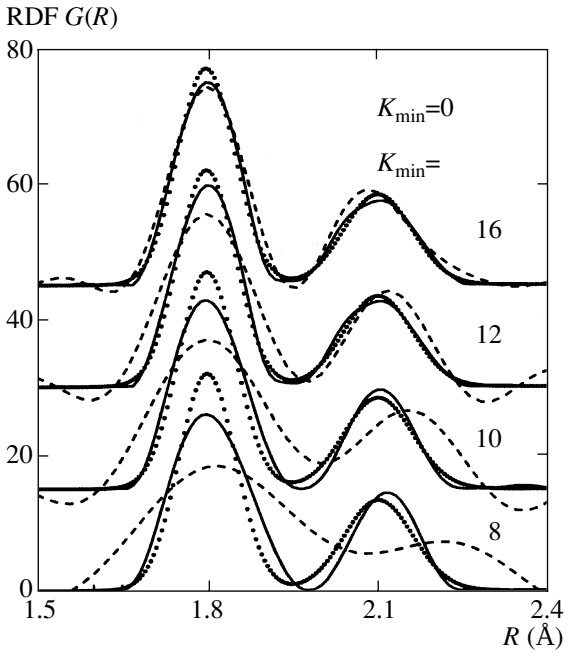

Fig. 18. The radial distribution function (RDF) obtained by the (dashed lines) splice method and (solid lines) model independent method at $k_{min} = 0$ for various values of the upper limit k_{max} of the EXAFS signal. The dotted line is the model RDF.

RDF in an analytical form, e.g., Gaussian curve, or in the form of cumulative expansion [65-68]; (ii) model independent methods for *ab initio* reconstruction of the RDF such as the regularization method [69-71], free-style Monte Carlo method [72], inverse Monte Carlo method [73], and nonlinear conditional fitting [36-38]; and (iii) the splice method [74, 75].

The splice method stands out because it is based on the model independent procedure for inverting the EXFAS signal. But it uses the restricted cumulative expansion to reconstruct the EXAFS signal in the range from zero to the lowest experimentally accessible value of the wave number. All three groups of methods are presented in Fig. 13 and are implemented in the EDA package [36-38].

The first group is represented by the EDAFIT code, which is based on the fast algorithm of conditional least-squares nonlinear fitting [36, 38] and on the multicomponent Gaussian/cumulative model in the single-scattering approximation [33–35]:

$$\chi(k) = \sum_i (N_i S_0^2)/(kR_i^2) F_i(\pi, k, R_i)$$
$$\times \exp[-2\sigma_i^2 k^2 + (2/3)C_{4i}k^4 - (4/45)C_{6i}k^6]$$
$$\times \exp[-2R_i/\lambda(k)] \sin[2kR_i - (4/3)C_{3i}k^3$$
$$+ (4/15)C_{5i}k^5 + \Psi_i(\pi, k, R_i)],$$

where N_i is the number of atoms in the ith group spaced at the distance R_i from the absorbing atom; σ_i is the standard deviation of the distance; C_{3i}, C_{4i}, C_{5i}, and C_{6i} are the distribution cumulants providing approximation of the contribution from the anharmonic vibrations and/or non-Gaussian disorder; $F_i(\pi, k, R_i)$ is the amplitude of the backward scattering from the ith-group atoms; the phase shift $\Psi_i(\pi, k, R_i) = \psi_i(\pi, k, R_i) + 2\delta_l(k) - l\pi$, where the photoelectron orbital angular momentum l is equal to 1 for K and L_I edges and to 2 or 0 for $L_{II, III}$ edges, includes the contributions $2\delta_l(k)$ and $\psi_i(\pi, k, R_i)$ from the absorbing and scattering atoms, respectively; $\lambda(k)$ is the mean free path of the photoelectron; and the factor $S_0^2 = 0.6$–0.95 specifies that change in the wave function of $n - 1$ electrons, which accompanies excitation of the nth electron. The model contains free structure parameters N_i, R_i, σ_i, C_{3i}, C_{4i}, C_{5i}, and C_{6i}. The amplitude $F_i(\pi, k, R_i)$ and phase shift $\Psi_i(\pi, k, R_i)$ can be taken from tables in [76, 77], calculated by the available codes EXCURE [40, 41], FEFF [42-45], GNXAS [46-49], MSCALC [78], or MSXAS [79, 80], or extracted from the EXAFS spectrum of the standard compound [81]. The last two approaches are preferable. The best result can be achieved by fitting the calculated amplitude and phase shift for the standard compound, which makes it possible to simultaneously obtain accurate and noiseless functions $F_i(\pi, k, R_i)$ and $\Psi_i(\pi, k, R_i)$. Note that the amplitude and phase shift that are calculated with the complex exchange-correlation potential, e.g., the Hedin-Lundquist potential [42, 78] automatically involves the contribution from inelastic photoelectron scattering, which determines the mean free path $\lambda(k)$ of the photoelectron. In this case, the factor $\exp[-2R_i/\lambda(k)]$ should be excluded from the model. This model is applicable only to compounds whose RDFs can be represented as several Gaussian or Gaussian-like peaks.

The splice method [74, 75] is based on determining the RDF $G(R)$ by inverting the reduced EXAFS function $\chi'(k)$ by taking the Fourier transform:

$$G(R_i) = \int \chi'(k) \exp(-2ikR_i) dk,$$

where $\chi'(k) = \chi(k) k R_i^2 \exp[i\Psi(\pi, k, R_i)]/\{S_0^2 F(\pi, k, R_i)\exp[-2R_i/\lambda(k)]\}$ and integration is performed from zero to infinity. Because the experimental EXAFS signal is usually determined from $k_{min} > 0$ to $k_{max} \approx 10$–20 Å^{-1}, and its amplitude decreases with increasing the wave number k, we set $\chi(k > k_{max}) = 0$ in the integral. The $\chi(k < k_{min})$ values are extrapolated by using the cumulative model, whose parameters are found from the best fit to experimental data from k_{min} to k_{max}. The accuracy of determining the RDF is restricted by (i) the applicability of the cumulative approximation in the range $0 < k < k_{min}$ and (ii) the magnitude of the experimental EXAFS signal at $k = k_{max}$. Indeed, if $|\chi(k_{max})| \gg 0$, the cutoff of the function $\chi(k)$ at $k = k_{max}$ results in distortion of the desired RDF in integration. Figure 18 illus-

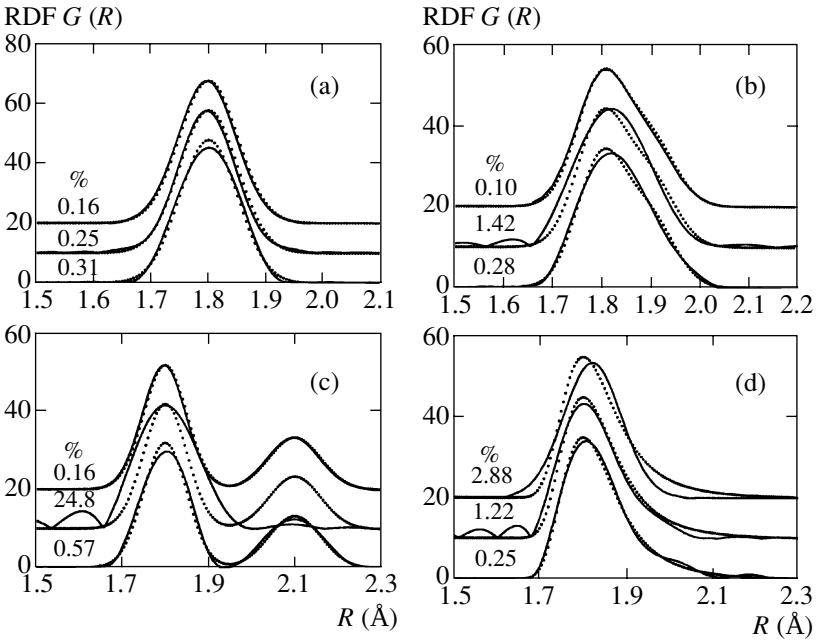

Fig. 19. The radial distribution functions (RDFs) extracted from the EXAFS signal by employing the model RDF (dotted line), the Gaussian model (upper solid lines), cumulative-model (middle solid lines), and model-independent technique (lower solid lines). The numbers near the lines are the values of the quantity

$$\varepsilon = 100\% \frac{\sum (\Phi PP_{\text{cal}} - \Phi PP_{\text{mod}})^2}{\sum (\Phi PP_{\text{mod}})^2}$$

characterizing the agreement between the corresponding RDF and model one.

trates this effect by the example of the model RDF in the form of two Gaussian peaks with the parameters $N_1 = 2$, $R_1 = 1.8$ Å, $\sigma_1 = 0.05$ Å, $N_2 = 1$, $R_2 = 2.1$ Å, and $\sigma^2 = 0.06$ Å. It is seen that a decrease in the upper integration limit $k_{\max}$, which is equivalent to an increase in the EXAFS-signal amplitude at $k = k_{\max}$, leads to an increase in the deviation of the resulting RDF from the model one. In the EDA package, the splice method is implemented in EDAFT and EDAPLOT codes.

The model independent methods of *ab initio* reconstruction of RDF is realized in the EDAEDF code of conditional nonlinear fitting [36-38]. For arbitrary RDF, the EXAFS signal is represented as [82, 83]

$$\chi(k) = S_0^2 \int [G(R)/(kR^2)] F(\pi, k, R) \times \sin[2kR + \Psi(\pi, k, R)] dR,$$

where an arbitrary input RDF $G(R) = 4\pi R^2 \rho_0 g(R)$ corresponds to the number of atoms in the spherical layer from R to $R + dR$ around the absorbing atom and is specified from $R_{\min}$ to $R_{\max}$ with the step $\Delta R \le 1/(2k_{\max})$. The iteration procedure is used to determine the desired RDF by minimizing the quantity

$$S = \sum_k [\chi_{\text{mod}}(k) - \chi_{\text{exp}}(k)]^2$$

with additional constrants (i) $G(R) \ge 0$ and (ii) $G(R)$ should be a differentiable function. If it is necessary, extra conditions can be imposed on the $G(R)$ area magnitude, i.e., on the total coordination number. In the most practical cases, the RDF of the first coordination sphere vanishes at the ends of the interval $[R_{\min}, R_{\max}]$, which allows correct integration. This method imposes no restrictions on the RDF form.

Below, we will present several examples of applying the above methods for reconstructing the RDF in model and real systems. Figure 18 shows the results of the model independent method and the splice method. It is seen that the boundedness of the EXAFS signal affects the first method considerably less. In fact, it broadens the RDF peaks, which is related to a decrease in the resolution in the R space because of the shortening of the EXAFS signal.

Figure 19 shows the results of the Gaussian and cumulative models, as well as of the model independent method. The model RDFs were chosen so as to reproduce the $G(R)$ forms frequently presented in actual compounds: a single Gaussian peak ($N = 1$, $R = 1.8$ Å, and $\sigma = 0.06$ Å); two nonresolved Gaussian lines ($N_1 = 2$, $R_1 = 1.8$ Å, $N_2 = 1$, $R_2 = 1.9$ Å, and $\sigma_1 = \sigma_2 = 0.06$ Å); two Gaussian peaks ($N_1 = 2$, $R_1 = 1.8$ Å, $\sigma_1 = 0.05$ Å, $N_2 = 1$, $R_2 = 2.1$ Å, and $\sigma_2 = 0.06$ Å); and an asymmetric RDF similar to that observed in superionic materials. Figure 19 demonstrates that, when the distribution form differs from the analytical model, discrepancies in the position, intensity, and width of RDF peaks are observed: the Gaussian model fails to reproduce the

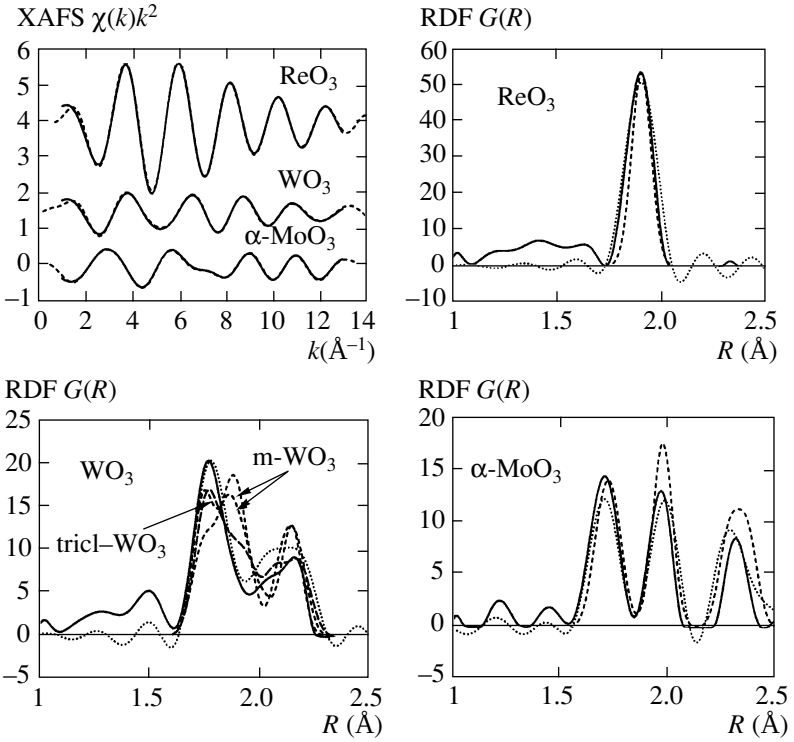

Fig. 20. (a) Model independent EXAFS signals (solid lines) $\chi(k)k^2$ from the first coordination sphere of rhenium in ReO_3 (rhenium L_3 edge), tungsten in WO_3 (tungsten L_3 edge), and molybdenum in α-MoO_3 (molybdenum K edge) compared to the corresponding experimental data (dashed lines), (b)-(d) the radial distribution functions (RDFs) of the first coordination sphere obtained by the (dotted lines) splice method, (solid lines) model independent method, and (dashed lines) using x-ray and neutron diffraction data.

asymmetric RDF, whereas the cumulative model poorly reproduces the two-Gaussian distributions. Only the model independent method reproduces all RDF types equally well.

Figure 20 shows the application of the splice method and the model independent approach to three actual crystalline compounds-trioxides of rhenium, tungsten, and molybdenum. The structural RDF peaks that are reconstructed by both methods agree well with each other and with the RDFs reconstructed from the x-ray and neutron diffraction data. Moreover, the resulting RDFs for tungsten trioxide enable us to unambiguously distinguish the triclinic (tricl-WO_3) and monoclinic (m-WO_3) modifications, which can coexist at room temperature in an experiment. Experimental data and model independent calculation of the EXAFS signals from the first coordination sphere are in very good agreement with each other. Nonstructural peaks in the short-distance range in the RDF (see Fig. 20) reflect errors in experimental EXAFS signals. The splice-method RDFs in some ranges have negative values originating in the Fourier transform, because the experimental-spectrum interval is too short.

Several models of the EXAFS signals often provide close agreement with experimental data, which leads to inconclusive interpretation. Moreover, employment of the multicomponent Gaussian or cumulative models brings about the problem of choosing the minimum number of components providing the adequate reproduction of an experimental signal. To resolve this problem, it is convenient to employ the Nyquist and Fisher criteria [38, 84]. The Nyquist theorem restricts the maximum number of model parameters that can be used to analyze an experimental signal specified in the intervals Δk and ΔR:

$$M_{\max} = (2\Delta k \Delta R)/\pi + 2.$$

In particular, for the EXAFS signal from the first coordination sphere of the rhenium trioxide, we have $\Delta k = (13 - 1)$ Å^{-1} = 12 Å^{-1} (see Fig. 37) and $\Delta R = (1.9 - 0.7)$ Å = 1.2 Å (see the first-peak range in Fig. 16) and, therefore, $M_{\max} \approx 11$. This number is obviously greater than the actual number (three) of the parameters (N, R, and σ) needed for describing the first rhenium coordination sphere consisting of six equidistant oxygen atoms. The application of the Fischer criterion to the dispersive analysis makes it possible to find the model that matches the experimental data with the minimum number of parameters. Let M_1 and M_2 ($M_2 > M_1$) be the numbers of parameters of models $\chi_1(k)$ and $\chi_2(k)$, respectively. In this case, the variances D_1 and D_2 are

$$D_j = [M_{\max}/(n(M_{\max} - M_j))]\sum_i [\chi(k_i) - \chi_j(k_i)]^2,$$

$$j = 1, 2, \quad i = 1, \ldots, n,$$

and, according to the Fisher $F_{0.95\%}$ criterion, the model $\chi_2(k)$ is accepted when $D_1/D_2 > F_{0.95\%}$. The $F_{0.95\%}$ quan-

tity is tabulated [84]. In the EDA package, the dispersive analysis is implemented in the FTEST code.

Numerous experiments give the following averaged estimates for the accuracy of the basic structure parameters in the first coordination sphere: $\Delta R \approx 0.01$ Å for the interatomic distances R_j, $\frac{\Delta N}{N} \geq 10\%$ for the number of atoms, and $\frac{\Delta\sigma}{\sigma} \geq 20\%$ for the Debye-Waller factor. For the next spheres, the accuracy sharply deteriorates and is substantially determined by the structure type and approximations in use. In the most cases, the EXAFS function provides the most accurate description of the microscopic structure of a condensed state near the absorbing atoms up to the distances 4–6 Å and not greater than 10–15 Å.

3. BASIC EXAFS-SPECTROMETER SCHEMES AT THE SYNCHROTRON RADIATION BEAM

We describe the experimental procedures of measuring the EXAFS function with fixing various channels of excitation of a solid by incident x-ray radiation.

(i) Measurement of the transmission function when the total transmission coefficient $T(E_\gamma)$ for radiation with the specified energy $E_\gamma = \omega$ through an object of thickness L_x is obtained. Then, the function $T(E_\gamma)$ is used to reconstruct the absorption coefficient μ as a function of the photon energy by the formula $L_x\mu = \ln\left(\frac{I_0(E_\gamma)}{I(E_\gamma)}\right)^{1/x}$, where $I_0(E_\gamma)$ and $I(E_\gamma)$ are radiation intensities with and without a sample. Figure 21 shows the transmission scheme of measurement of the EXAFS spectrum [27].

(ii) Determination of the EXAFS function by detecting the decay channels of the state excited by the absorbed photon (fluorescence, yield of the secondary electrons, and photoluminescence).

In the transmission measurement of the EXAFS function, the absorption coefficient μ_x of the sample under investigation is determined with the accuracy $(\Delta\mu_x)^2 = \frac{3.223}{(I_0)}(\mu_x + \mu_m)^2$ [24], where I_0 is the incident radiation intensity in kilowatts per second, and μ_m is the absorption coefficient of the matrix in which the sample is placed. The absorption coefficients are $\mu_m = N_m\sigma_m$ and $\mu_x = N_x\sigma_x$, where N_m and N_x are the numbers of atoms in the matrix and sample, respectively; and σ_m and σ_x are the cross sections for absorption of photons by the matrix and sample, respectively.

The formula for $\Delta\mu_x$ was derived under the assumption that the sample thickness L_x is chosen so that the error $\frac{\Delta\mu_x}{\mu_x}$ is minimal, which gives $L_x = \frac{2.557}{\mu_x}$. For the second measurement scheme, when one determines the secondary-particle yield accompanying the absorption of x-ray radiation [24], we have

$$(\Delta\mu_x)^2 = \frac{1}{(I_0)}\left(\frac{2\mu_x}{FL_x}\right),$$

where F is the total efficiency of detecting secondary particles, $F \leq 1$ and L_x is the sample thickness.

For the exploration of biological samples consisting of an absorber and the object under investigation with the absorption coefficients μ_m and μ_x, respectively, $\mu_x \ll \mu_m$, and in the transmission-scheme measurement, the signal-to-noise ratio is

$$(S/N) = (I_0 t)^{1/2} \times 2e^{-1}\frac{\mu_x}{\mu_m}$$

for the optimal sample thickness so that $\mu_m L_x = 2$.

In particular, for the incident radiation intensity $I_0 \approx 10^{11}$ kW/s, $t = 1$ s, and $S/N = 3$, the equation yields $\frac{\mu_x(\omega)}{\mu_m} = 1.3 \times 10^{-5}$. This means that this regime provides measurements for atoms whose content is 10^{-3}% of the basic component.

For measurements in the fluorescence mode, when the fluorescence signal of the energy ω_F is recorded by a narrow-band detector, the signal-to-noise ratio is [24]

$$S/N = \frac{I_0 fF\mu_x(\omega)\Omega}{(\mu_m(\omega) + \mu_m(\omega_F)) \times 4\pi},$$

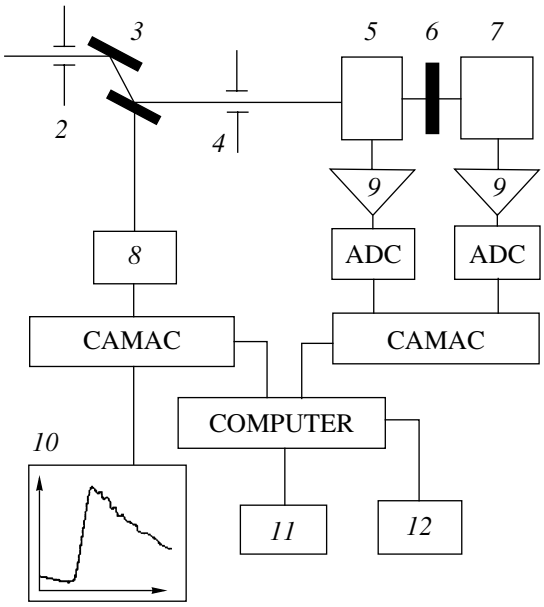

Fig. 21. Block diagram of an experimental EXAFS spectroscopy station: (*2*) and (*3*) collimators, (*3*) monochromator, (*5*) monitor, (*6*) sample, (*7*) detector, (*8*) step-by-step motor, (*9*) amplifier, (*10*) display, (*11*) terminal, (*12*) plotter printer.

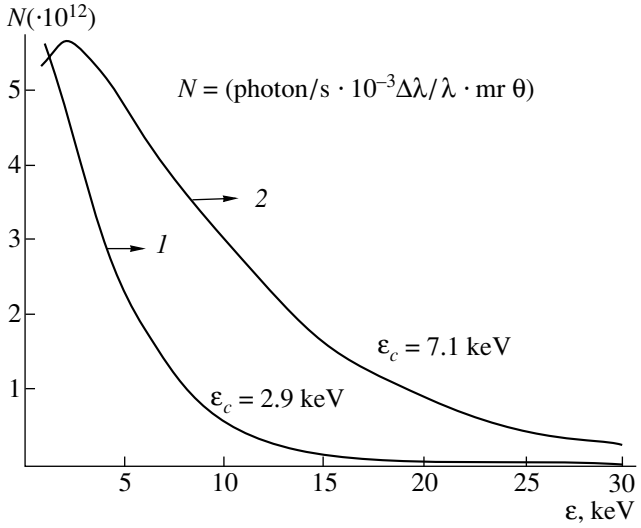

Fig. 22. The spectral brightness N of the two SR sources: (*1*) DCI (France) with E_e = 1.8 GeV and critical photon energy E_c = 2.9 keV and (*2*) Siberia-2 (Russia) with E_e = 2.5 GeV and E_c = 7.1 keV.

where f is the fluorescence yield, F is the detector sensitivity, and Ω is the solid angle in which secondary radiation is detected.

For $I_0 = 10^{11}$ photons/s, t = 1 s, $F\Omega/4\pi = 0.01$, and $f = 0.1$, estimation for the fluorescence mode yields $\frac{\mu_x}{\mu_m} = 4 \times 10^{-8}$, which is three orders of magnitude as large as the value obtained for transmission measurements. As follows from the formulas for statistical accuracy, the radiation source intensity is primarily responsible for the time required for accumulating the necessary statistics. For laboratory EXAFS spectrometers used with radiation from x-ray tubes of the intensity of about 10^5 kW/s per line with the resolution δE = 5–6 eV, the time of accumulating the EXFAS spectrum is 10–12 h [27].

Table 2. The Darwin width Ω_x of the Bragg reflexes, energy resolution $\Delta E/E$, the integral reflectance I of perfect crystals of silicon, germanium, and α quartz for λ = 1.5 Å [33]

Crystal	*hkl*	Ω_x second of arc	$\Delta E/E \times 10^5$	$I \times 10^6$
Silicon	111	7.395	14.1	39
	220	5.459	6.04	29.7
	311	3.192	2.9	16.5
	400	3.6	2.53	19.3
Germanium	111	16.338	32.6	85.9
	230	12.44	14.46	67
	311	7.23	6.92	37.4
	400	7.95	5.94	25.4
α quartz	100	3.798	10.0	18.8
	101	7.453	15.26	40.9
	110	2.512	3.69	12.2
	200	2.252	2.81	11.5

Considerable advancement in EXAFS spectroscopy have been achieved by using SR with spectral brightness far exceeding that of continuous-operation sources based on x-ray tubes. Figure 22 shows the parameters of brightness for two SR sources: DCI, France, E = 1.8 GeV, I_e = 200 mA and Siberia-2, Russia, E_e = 2.5 GeV and I_e = 200 mA. Radiation from these sources allows the measurement of the EXAFS spectra with the accumulation time from 10 to 10^{-3} s depending upon the spectrometer scheme.

To measure the EXAFS function $\chi(E_\gamma)$ in both the transmission and fluorescence schemes, it is necessary to monochromatize E_γ radiation incident on a sample with the energy resolution ΔE_0, which is determined by the dimension R_j of the first coordination sphere. The necessary resolution for most objects under investigation should be $5 \le \Delta E_0 \le 12$ eV.

To monochromatize the continuous SR spectrum, the Bragg reflection of x-ray radiation from crystals with various interplanar spacings $2d_{hkl}$ is used. The wavelength and reflection angle θ are related as $2d\sin\theta = n\lambda_x$, where n is the order of reflection. The energy spread ΔE is determined by the angle of the cone of reflected and incident radiations [27]:

$$\frac{\Delta E}{E} = \cot\theta\Delta\theta,$$

where $\Delta\theta$ is the angular dispersion of radiation reflected from a crystal.

For a monochromator, $\Delta\theta$ is the sum of the three terms: the angular spread $\Delta\theta_s$ of incident radiation with respect to the Bragg angle (θ_s is determined by the channel acceptance and the dimension of the radiation source); the angular spread $\Delta\theta_m$ determined by the input monochromator aperture; and the angular width of the reflected radiation (Darwin width) $\Omega_x(\lambda_x) = \frac{2}{\sin\theta}\frac{r_0\lambda_x^2}{\pi v}F_@$, where $F_@$ is the structure factor of the crystal, v is the crystal-cell volume, and r_0 is the classical electron radius. The Darwin curve determines the limiting monochromator resolution $\frac{\Delta E}{E} = \Omega_x\cot\theta$.

Table 2 presents the intrinsic widths of the Bragg reflexes, energy resolution $\Delta E/E$, the integral reflectance I of perfect crystals of silicon, germanium, and α quartz for λ = 1.5 Å [33].

To reduce the Darwin width of a reflex, asymmetric diffraction is used; i.e., the plane on which radiation is incident is at the angle α to reflecting planes. In this

case, the reflex width is $\Omega_\alpha = \Omega_x\sqrt{b}$, where $b = \frac{\sin(\theta-\alpha)}{\sin(\theta+\alpha)}$.

In actual experiments, the dispersive plane is vertical and the angular width of SR governs the monochromator resolution. In particular, for the Siberia-2 storage ring with electron energy $E = 2.5$ GeV, the half width of the angular distribution of SR is $\Delta\theta_{SR} = \frac{1}{\gamma} \approx 2\times10^{-4}$ rad for the wavelength $\lambda \approx \lambda_{cr}$. Thus, the angular width of the incident radiation is about one order of magnitude as large as the Darwin width for an Si (111) crystal. Therefore, to increase resolution, the incident SR beam should be collimated by input monochromator slits.

A two-crystal monochromator scheme is extensively used in EXAFS spectroscopy. The first crystal serves as a direct monochromator and the second crystal filters higher harmonics at small angular rotation about the first crystal within the Darwin width of the reflection curve, because the reflection curve for the second and third orders is shifted by several seconds of arc. Figure 23 shows the reflection spectra in the first and second orders [23] and demonstrates that higher harmonics exhibit both the shift of the rocking curves and a decrease in the reflection width. These features enable one to use mirrors for grazing incidence angles for separating higher orders of the Bragg reflection.

As was mentioned above, the monochromator resolution of absorption spectroscopy in the XANES and EXAFS regions are governed by different physical processes.

(i) For XANES, the resolution should be no worse than the intrinsic line width determined by the half life of the core hole level, $\Delta E_\tau = 2\times10^{-4}E_{BE}$, where E_{BE} is the binding energy of the level B; $\Delta E = 1.4$–2 eV for the energies 7-10 keV.

(ii) For EXAFS, the monochromator resolution ΔE_0 should be better than the fine-structure energy scale $\Delta E_{EXAFS} = \frac{\hbar^2|\Delta k|}{m} = \frac{\hbar^2\pi|k_{min}|}{2mR_j}$, where k_{min} is the wave number of an electron with minimal energy 2 Å^{-1}, R_j is the radius of the first coordination sphere; 5 eV $\le \Delta E_{EXAFS} \le$ 12 eV for 2 Å $\le R_j \le$ 5 Å.

Figure 21 shows the block diagram of the experimental set for EXAFS spectroscopy at the SR beam from the DCI storage ring with the energy $E_e = 1.8$ GeV [50]. This set was employed for examining the structure of oxide compounds. The set is based on a two-crystal parallel-installed monochromator and the resolution $\Delta E/E \approx 10^{-4}$ in the range 5–15 keV. The transmission measurement of the EXAFS function is carried out by two proportional chambers, which detect the radiation fluxes I_0 and I_x in front of and behind the sample, respectively. The absorption coefficient is determined by the formula

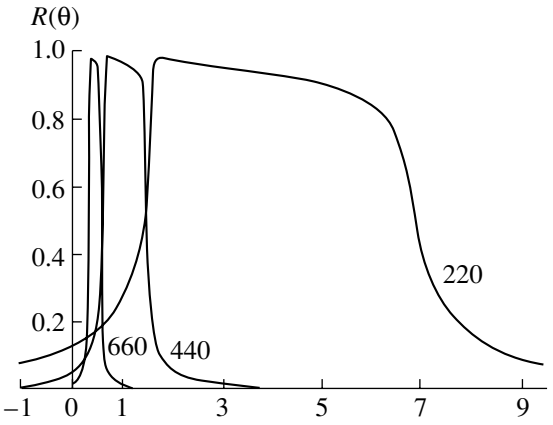

Fig. 23. The x-ray reflection spectra from Si(220) silicon for various reflection orders at λ = 1.5 Å.

$$L_x\mu_x(E) = \ln(I_0/I_x).$$

The measurement of the entire EXAFS spectrum requires about 10 min and is carried out by sequential energy scanning.

The original scheme of the EXAFS spectrometer without mechanical scanning in the wavelengths (EXAFS energy-dispersive spectrometer) was first presented in [85]. It is based on the focusing of x-ray radiation at the sample in the energy range ΔE by using a bent monochromator crystal. In this case, the spectrum of passing radiation is spatially decomposed near the point of energy focusing and is recorded by a detector with spatial resolution.

The energy-dispersive EXAFS spectrometer has the following advantages over the classical one.

(i) The absence of mechanical scanning; measurement of the energy dependence of the absorption spectrum is reduced to the measurement of the spatial distribution of x-ray radiation passing through a sample.

(ii) At the minimal measurement time $t \approx 3$ ms, which is ensured by current position-sensitive solid detectors, this scheme makes it possible to expose the structure of solids *in situ* to various external fields.

(iii) The possibility of focusing radiation at a sample to hundreds of micrometers enables one to place the sample within the high-pressure chamber and to explore the pressure effect on the short-range order.

At present, many SR research centers are equipped with energy-dispersive EXAFS spectrometers [86, 87], which are employed for numerous investigations on physics and chemistry of catalysts, electrochemical processes, cryogenic crystals, magnetic structures, and phase transitions [88-90].

4. ENERGY-DISPERSIVE EXAFS SPECTROMETER

At present, a specialized SR source was commissioned by the Kurchatov Institute. The parameters of

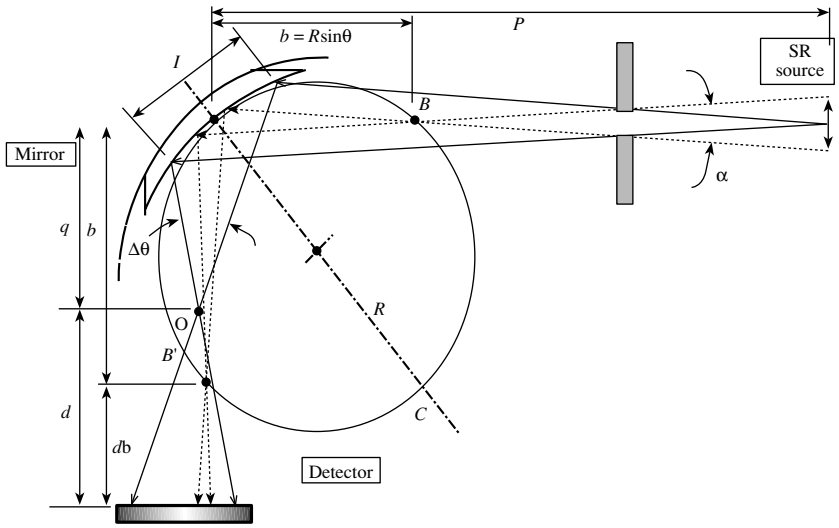

Fig. 24. The optical scheme of the energy-dispersive EXAFS spectrometer.

SR from its bending magnet are the following: the critical photon energy E_c = 7.1 keV; maximum brightness $B = 2 \times 10^{14}$ photons/(s mm^2 mrad^2) into the band $\Delta\lambda/\lambda = 10^{-3}$ at the accumulated-electron current I_e = 100 mA; and its spectral brightness is shown in Fig. 22.

A set for energy-dispersive EXAFS spectroscopy is under construction at one of the source channels [87]. Figure 24 shows the optical scheme of the energy-dispersive spectrometer whose basic units are as follows:

(i) a bent-crystal monochromator with the length l and the varying radius of curvature R;

(ii) an optical bench with the rotation axis coaxial with the monochromator axis; and

(iii) a one- or two-dimensional (depending upon the problem under investigation position-sensitive detector).

The beam dimension at the entrance to the channel is S = 6 mm and the length of the beam transport channel to the monochromator is p = 20 m. An x-ray beam incident on a crystal is formed by a horizontal slit situated ahead of the monochromator entrance. The operating energy range of x-rays is determined by the parameters of the silicon and germanium crystals used in the spectrometer.

Table 3 presents the parameters of the crystals, energy range, and energy resolution for the Bragg scheme. The energy resolution δE of the spectrometer is determined by the formula $\delta E = \delta\theta E \cot\theta$, where the total angular resolution $\delta\theta$ of the entire optical scheme is the sum of following three terms [85]. First, the angular resolution $\delta\theta_1$ determined by the spatial resolution ρ of the detector located at the distance d from the polychromatic focus (PF) is represented as

$$\delta\theta_1 = \frac{\rho}{\sin\theta}\frac{q}{d}\left(\frac{1}{R} - \frac{\sin\theta}{p}\right) = Q(\rho/d),$$

$$Q = \frac{1}{2}\frac{1 - b/p}{1 - b/2p},$$

where q is the distance from the crystal center to the PF. Second, the angular resolution $\delta\theta_2$ corresponding to the finite size S of the radiation source is calculated as

$$\delta\theta_2 = Q\alpha\left(1 - \frac{b-q}{d}\right).$$

Here, $\alpha = S/(p - R\sin\theta) = S/(p - b)$, where θ is the Bragg angle, p is the distance from the radiation source to the crystal, and R is the radius of curvature of the crystal. Third, the angular resolution $\delta\theta_3$ originating from the finite thickness δ of the crystal is determined by the formula

$$\delta\theta_3 = Q\frac{\delta\cos\theta\sin\theta}{d}\frac{1 - \dfrac{b-\theta}{p}}{1 - \dfrac{b}{p}}.$$

The total angular resolution also includes the Darwin angular width Ω of the rocking curve. As a result, we have

$$\delta\theta^2 = \delta\theta_1^2 + \delta\theta_2^2 + \delta\theta_3^2 + \Omega^2,$$

Table 3

Crystal	Energy range, keV	Resolution $\delta E/E$
Si(111)	5–15	$\cong 10^{-4}$
Si(311)	7–30	$\cong 10^{-4}$
Asymmetric Si(311), a = –12	7–30	$< 10^{-4}$

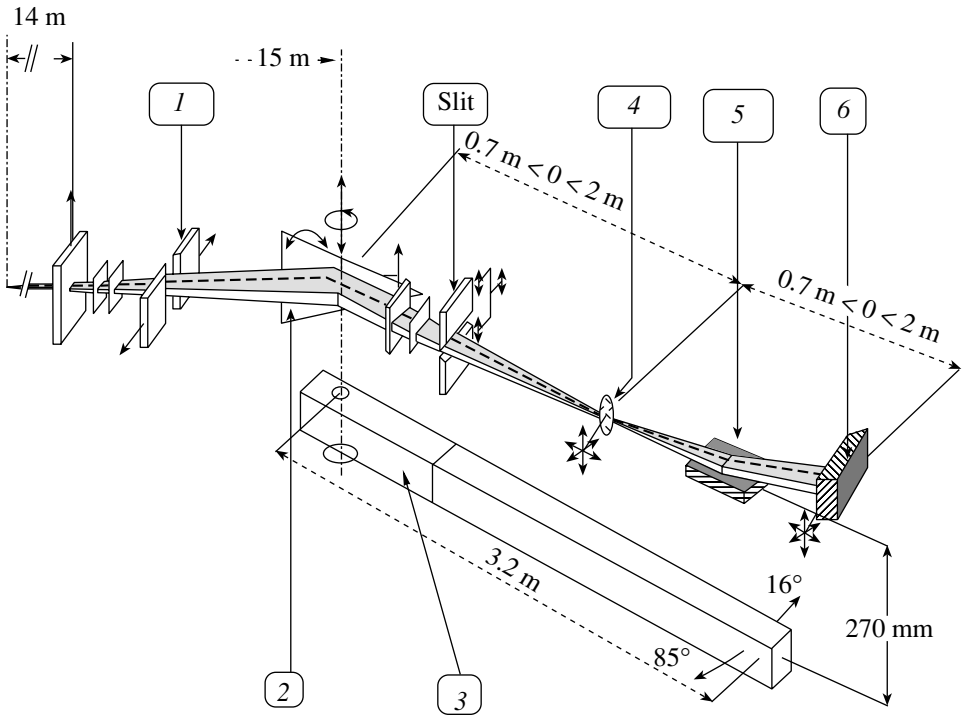

Fig. 25. Block diagram of the energy-dispersive EXAFS spectrometer: (*1*) input forming optics, (*2*) monochromator with triangular Si crystal and bending device, (*3*) optical bench on aerostatic supports, (*4*) cryostat and high-pressure chamber, (*5*) mirror unit, (*6*) cryogenic two-dimensional position-sensitive detector.

$$\delta\theta^2 = [\rho^2 + (\alpha\delta b)^2 + (\delta\sin\theta\cos\theta)^2] \times\left(1 - \frac{b-\delta b}{p}\right)^2 \frac{1}{(1-b/p)^2}\left(\frac{Q}{d}\right)^2 + \Omega^2,$$

where $\delta b = d - (b - q)$ is the deviation of the detector position for various photon energies.

The angular resolution is minimal at $\delta b_{\min} = \rho^2/\{\alpha^2(b-q)\}$, which is achieved at $(d+q)_{\min} = b + \rho^2/[\alpha^2(b-q)]$. For the parameters $\alpha = 3 \times 10^{-4}$ for a given optical channel, the detector resolution $\rho = 50$ μm, $b - q \cong \sin\theta R/2$ for CuK_α energies and Si(111) crystal, $\theta = 13°$, and $R = 697$ cm, we obtain $\delta b_{\min} \cong 3$–4 cm. In particular, for the CuK_α energy, monochromator-detector distance $L = (d+q)_{\min}$, and Si(111) crystal, we obtain the optimal resolution $\delta E = 2$ eV. For the Si(311) crystal and energy $E = 10.3$ keV, the measured resolution is $\delta E \cong 1.2$ eV.

An analysis of the energy-resolution expression demonstrates that the determining factor is the horizontal radiating-region dimension S, which should be reduced. For an energy-dispersive EXAFS spectrometer, an important parameter is the energy range ΔE of measurement by the EXAFS spectrometer:

$$\Delta E = (l/R - l\sin\theta/p)\cot\theta,$$

where l is the monochromator-crystal length exposed to the x-ray radiation. The Bragg angle changes along the bent crystal and the radiation of the above-indicated range is focused at the PF. The ΔE value can vary from 200 to 800 eV for various radii of curvature. The region where energy focusing is performed has the dimension $\Delta L = \Delta\theta(d+q)_{\min} \cong R\sin\theta(l/R - l\sin\theta/p)$, $\Delta L = l\sin\theta =$ 4 cm for $\Delta E = 700$ eV.

For the EXAFS spectroscopy of radiation passing through a sample, the spectral measurements reduce to measuring the spatial distribution of the x-ray intensity at the focusing point, i.e., at the distance $(d+q)_{\min}$ from the monochromator. When a photodiode rule with 1024 elements and a 20-mm detection-region length is used, the intensity 0.4 eV/ps falls by at one detecting element.

Behind the PF, x-rays are dispersed in the horizontal plane along the radii of the circle with the center at the PF point O. If the optical bench with the rotation axis is equipped at the point O with the slit, which rotates about the point O, the slit will let the radiation of energy E_φ and spectral width $\delta E = \partial E/\partial\varphi\delta\varphi$, where $\delta\varphi$ is the angular width of the slit, pass for the angle φ.

The energy-dispersive optical scheme can be implemented in two variants of an EXAFS spectrometer [87].

Figure 25 shows the block diagram of the first variant, which is a transmission EXAFS spectrometer with time resolution. A sample is placed at the PF point O on the rotating optical bench. The sample unit can include the following devices:

(i) a circulated optical cryostat for the temperature range 4.7–300 K;

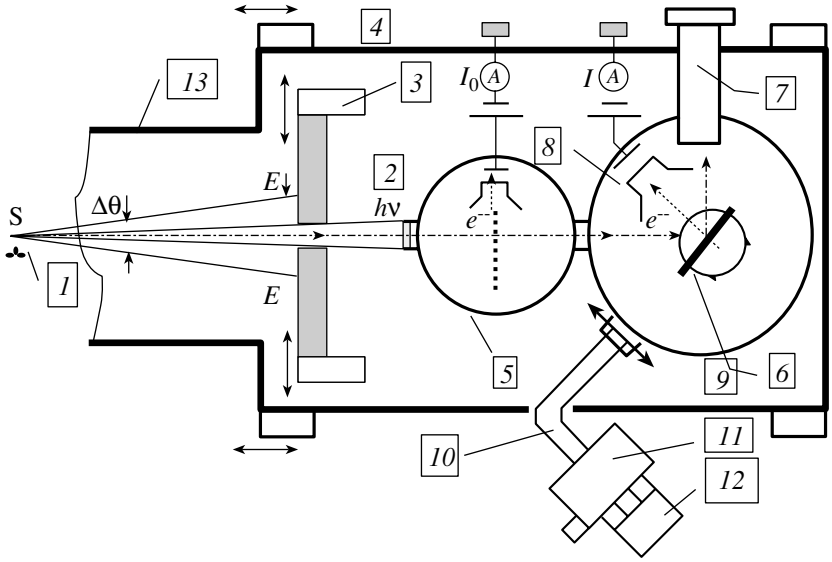

Fig. 26. Block diagram of the energy-dispersive EXAFS spectrometer with the fluorescence mode for measuring surface layers: (*1*) radiation source, (*2*) slit, (*3*) opening mechanism, (*4*) table rotating mechanism, (*5*) monitor chamber, (*6*) sample, (*7*) Ge (Li) detector, (*8*) counter of electrons, (*9*) lens, (*10*) x-ray guide, (*11*) monochromator, (*12*) photoelectric multiplier.

(ii) a high-pressure chamber with diamond anvils;

(iii) a magnetic-field chamber for measuring the magnetic dichroism;

(iv) a chamber for exploring the formation and growth of solid-phase species in aqueous and nonaqueous media; and

(v) a heating chamber for studying the structural-chemical transformations of solids in the range 20–600°C in isothermal and nonisothermal regimes.

Higher orders of x-ray radiation reflected from the monochromator are separated by a reflecting gold-plated mirror.

Figure 26 shows the block diagram of the second variant, which implies the surface EXAFS-spectrum measurements in the fluorescence mode. It is realized in an EXAFS spectrometer with energy variation by scanning in the angle φ through rotating the second optical bench along the arc corresponding to the energy range ΔE. In addition, the unit of measuring the optical radiation excited by x-ray radiation is mounted, which makes it possible to examine the structure and structural transformation of amorphous silicon films, as well as amorphous and poorly crystallized films of other substances-semiconductors, ferromagnets, ferroelectrics, etc.

Experiments at LURE, France, with the energy-dispersive spectrometer [86] demonstrated that the angular and energy spectra of scattering can simultaneously be measured in the scheme shown in Fig. 27. Investigations indicate that the resolution in the wave number $q = 2\pi\sin\theta/\lambda$ is $\delta q \cong 1.5 \times 10^{-3}$ Å^{-1}.

In summary, the energy-dispersive scheme allows measurements of the following spectra:

(i) EXAFS spectra with time resolution for observing the effect of various external actions on a sample with the energy resolution 2-4 eV in the energy range 5-25 keV;

(ii) EXAFS spectra and scattering spectra with the wave-number resolution $q \cong 10^{-1}$–10^{-3} Å^{-1}; and

(iii) EXAFS spectra in the fluorescence and optical modes of the surface layers.

4.1. Basic Units of the EXAFS Energy-Dispersive Station

To form an x-ray beam, the channel is equipped with a number of diaphragms and an exit slit varying from 1 to 30 mm. In addition, a focusing monochromator with a bent triangular crystal was designed for the EXAFS station and is shown in Fig. 28. The basic parameters of the spectrometer units are presented in Table 4.

To exploit the fully experimental advantages of the EXAFS energy-dispersive spectrometer with focusing of radiation at a sample with the dimensions 0.3×0.3 mm^2, a high-pressure chamber with diamond anvils is being constructed. Figure 29 shows the high-pressure cell and equipment necessary for its operation. The pressure P_{max} on a sample can vary with the diamond-anvil diameter, e.g., $P_{max} \sim 100$ kbar and = 1.6 Mbar for diamond ∅ = 0.8 and 0.2 mm, respectively.

For measurements of EXAFS spectra in the transmission and surface-reflection regimes, an x-ray position-sensitive detector with cryogenic cooling [91] was engineered on the basis of the multielement photodiode rule. Figure 30 shows the CuK_α and K_β spectra measured by this position-sensitive detector placed in the focal plane of the monochromator with a bent LiF crys-

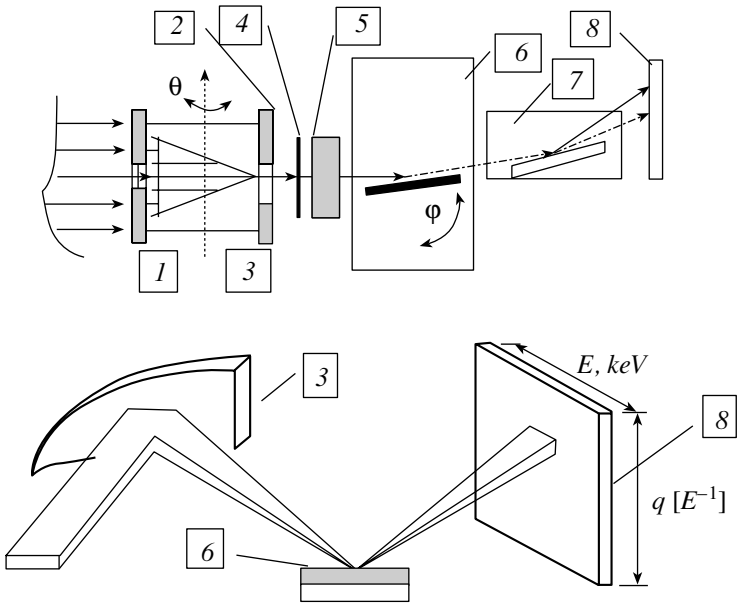

Fig. 27. Diagram of the energy-dispersive measurements of the angular and energy characteristic of scattered x-rays: (*1*) incoming SR beam, (*2*) output slit, (*3*) monochromator crystal, (*4*) beryllium window, (*5*) shutter, (*6*) sample unit, (*7*) mirror unit, (*8*) two-dimensional position-sensitive detector.

tal. The radiation source was an x-ray tube with a copper anode. Figure 31 shows the Cu K_{α_1} and K_{α_2} part of the spectrum.

At present, the basic units of the EXAFS energy-dispersive spectrometer are being mounted in the SR beam of the Siberia-2 storage ring at Kurchatov Institute.

5. LOCAL STRUCTURE OF THE OXIDES OF TUNGSTEN AND MOLYBDENUM

In this section, we discuss the application of the EXAFS method to explore the local structure of oxide compounds (crystals, glasses) and thin amorphous tungsten and molybdenum films. This class of materials is of considerable fundamental and applied interest.

Tungsten and molybdenum are transition elements whose physical properties are determined by the number of valence *d* electrons and the degree of their localization. The specific features of the oxides of tungsten and molybdenum are (i) the possibility of changing the valence of the metal ion under external action, which leads to a change in the optical and electrical properties of the compound containing these oxides, and (ii) the existence of mixed-valence compounds. In addition, these oxides can play the role of both a modifier and a frame-former in disordered structures (glasses and amorphous films). We emphasize that, in contrast to the classical frame-former oxides such as SiO_2, P_2O_5, and

Table 4. Parameters of the units of the EXAFS energy-dispersive spectrometer

Unit	Basic parameters
X-ray monochromator	
Crystal Si(111), Si(311):	width 50 mm, length up to 250 mm, thickness 1 mm
Crystal bending unit	Range 0–1 mm, discreteness 0.15 μm
Unit of crystal rotation about the *Z*-axis	without torsion: range –5–60°, discreteness 0.03°; with torsion: range 7′, discreteness 0.4′
Movable, granite optical bench on aerostatic supports	
Units for forming an SR beam	bench length 3.5 m, bench width 150 mm, angular rotation range 0–45°, rotation discreteness 20′, mismatch of the axes of the monochromator and the optical bench is less than 0.01 mm
Horizontal slit, vertical slit	opening range 0–40 mm, discreteness 0.1 mm
X-ray mirror unit	angular rotation ±10′, discreteness ±10′

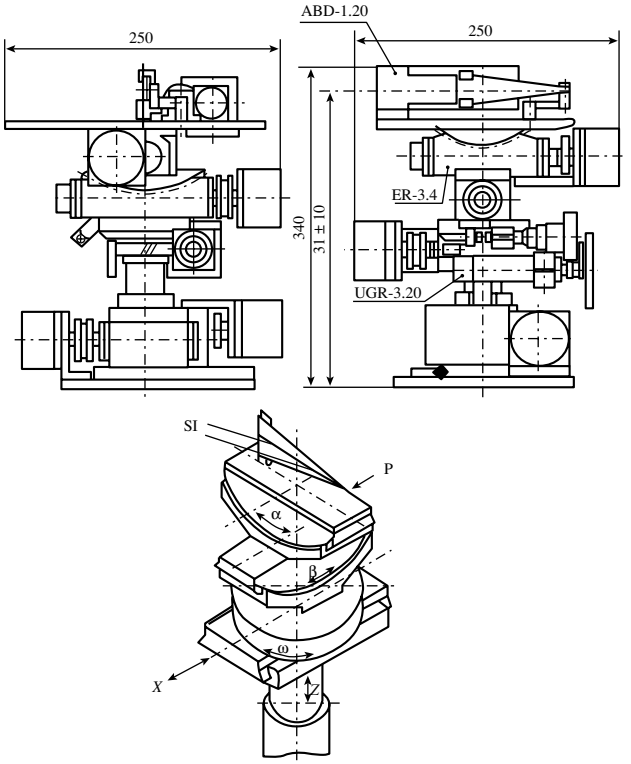

Fig. 28. Drawing of the focusing monochromator with a triangular crystal.

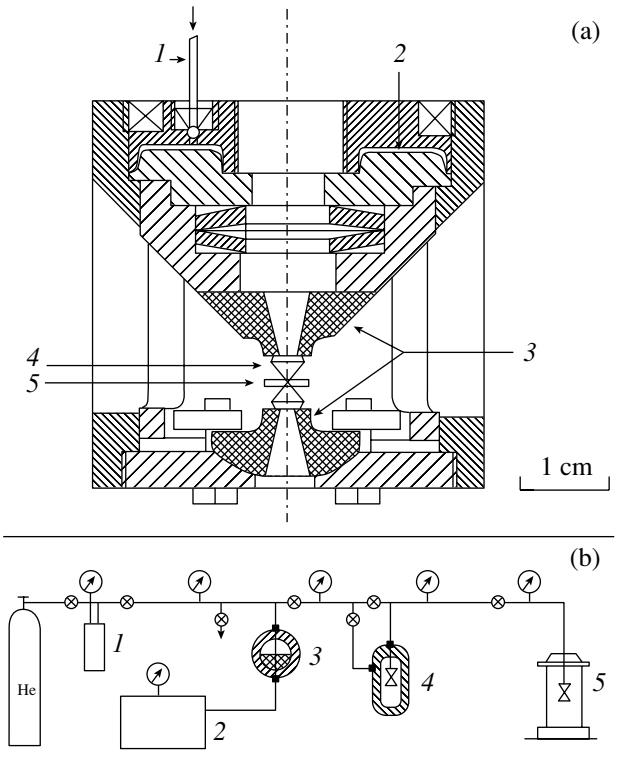

Fig. 29. (a) Membrane-type high-pressure cell with diamond anvils: (*1*) capillary for compressed-gas feed, (*2*) 0.2–0.3-mm membrane, (*3*) tungsten carbide supports for diamonds, (*4*) diamond anvils, (*5*) gasket with a sample; (b) gas unit for exerting pressure in the high-pressure chamber and filling the chamber with He: (*1*) clearing unit, (*2*) pumping unit NSVD-2500, (*3*) ball compressor, (*4*) unit for filling the high-pressure chamber with condensed helium, (*5*) the high-pressure chamber inside the cryostat.

B_2O_3, whose structure is based on polyhedrons where no more than four oxygen atoms are in coordination, the coordination of tungsten and molybdenum ions playing the role of a frame-former is often as high as octahedral. The listed properties motivate the use of the oxides of tungsten and molybdenum in electrochromic systems, catalysts, and sensors [92]. For this reason, deep insight into the relation between the physical properties and structure of the compound under investigation is of great importance. Application of the EXAFS method to this problem is justified by the fact that the majority of important practical properties of the oxide compounds of tungsten and molybdenum are governed by changes in the local atomic and electronic structures of metal ions.

In most of the compounds that will be considered below, the metal ion has the maximum degree of oxidation and the electronic configuration d^0. The basic structural element of these compounds, excluding $CaWO_4$, is the metal-oxygen octahedron $[MeO_6]$, where Me means W or Mo. It is well known [93] that d^0 transition-metal ions coordinated in an octahedron are usually displaced from the octahedron center; i.e., they occupy off-center positions. Comparison of the local environments of various d^0 ions (Ti^{4+}, Zr^{4+}, V^{5+}, Nb^{5+}, Ta^{5+}, Mo^{6+}, and W^{6+}) indicates that a distortion in the coordination octahedron $[MeO_6]$ increases with an increase in the formal ion charge and with a decrease in the ion radius [94]. The four causes of distortion were previously indicated [94].

The basic contribution, which is attributed to the second-order Jahn-Teller effect, comes from the electronic structure of a transition-metal ion. THe mixing of vacant *d* orbitals of cation and occupied *p* orbitals of ligands in a solid leads to the appearance of a set of various electronic configurations with closely spaced quasidegenerate energy levels, whose order is determined by the cation environment. Therefore, displacement of the cation from the octahedron center can remove degeneration and reduce the total energy of the system. The displacement of the metal ion from the octahedron center can be caused, besides the electronic second-order Jahn-Teller effect, by three structural factors [94]: (i) the type and number of chemical bonds with the nearest-neighbor atoms, (ii) structural incommensurability manifested as lattice stresses whose relaxation leads to the deformation of interatomic bonds, and (iii) the direct cation-cation repulsive interaction when two octahedrons are connected through a link or face.

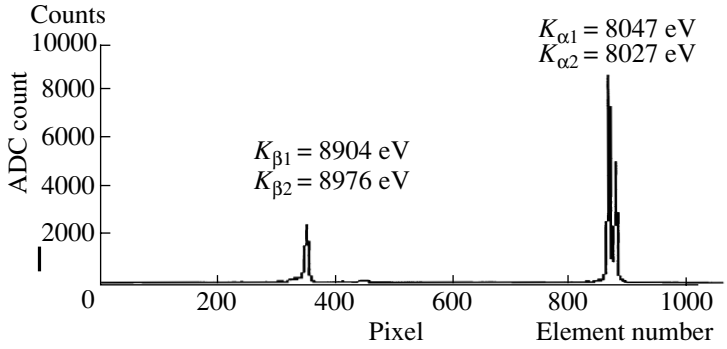

Fig. 30. Spectrum of a small-size x-ray tube with a copper anode. The operating voltage is 30 kV, the current is 25 mkA, and dispersing agent is SiO_2 (1340), R = 100 mm.

In each specific case, the degree of distortion of the coordination octahedron [MeO_6] depends both on the electronic effect magnitude and on the ability of the structure to accumulate distortions. The electronic and structural causes of distortion supplement each other and are not always easily separable. In conclusion, we note that the electronic effect alone does not determine the displacement direction of the metal ion from the octahedron center. This direction is governed by the structural causes of distortion or, in their absence, corresponds to one of the possible directions and, therefore, reduces the symmetry of the entire structure [94].

As the oxidation degree of the metal ion decreases to 5+, the *d* orbitals of this ion are filled to the configuration d^1, which results in a considerable change in the local structure. If a *d* electron is localized, the first-order Jahn-Teller effect [95] removes the degeneration and the local symmetry rises compared to the d^0 configuration up to tetragonal. For a nonlocalized *d* electron, the octahedrons [MeO_6] are completely symmetrized and the *d* electrons participate in the metallic conductivity. In both cases, the metal ion is at the octahedron center.

Thus, it is of considerable interest to determine the sensitivity of the EXAFS method to various types of distortion of the coordination octahedron [MeO_6]. To this end, the local structure of tungsten and molybdenum ions was examined in the tungsten-phosphorus (40% BaO + 40% P_2O_5 + 20% WO_3, 30% BaO + 30% P_2O_5 + 40% WO_3, 20% BaO + 20% P_2O_5 + 60% WO_3, and 34% P_2O_5 + 66% WO_3) and molybdenum-phosphorus (45% CaO + 45% P_2O_5 + 10% MoO_3, 40% CaO + 40% P_2O_5 + 20% MoO_3, 30% CaO + 30% P_2O_5 + 40% MoO_3, and 20% CaO + 29% P_2O_5 + 60% MoO_3) glasses, in polycrystalline compounds (monoclinic m-WO_3, cubic $Na_{0.6}WO_3$, $CaWO_4$, and α-MoO_3), and in polycrystalline β-MoO_3 and amorphous a-WO_3 and a-MoO_3 thin films [95, 96].

Experimental spectra were measured at the tungsten $L_{1,3}$ absorption edges and the molybdenum *K* absorption edge by using SR from the ADONE (Italy) and DCI LURE (France) storage rings [96, 97]. The measurements were carried out by the standard transmission method at room temperature. The x-rays were monochromatized by single Si(220) or double Si(311) monochromator crystals. The x-ray intensity was measured by two ionization chambers filled with krypton or argon.

Figure 32 shows the x-ray absorption spectra in the near-edge region. The tungsten L_3 absorption edge exhibits a pronounced intense peak, white line, corresponding to the allowed dipole transition from the $2p_{3/2}$(W) level to the quasibound mixed state 5*d*(W) + 2*p*(O) formed as a result of the hybridization of 5*d* orbitals of tungsten and 2*p* orbitals of oxygen. At the same time, the dipole transition from the tungsten 2*s* level at the L_1 edge is forbidden and its intensity depends strongly on the *p*-*d* mixing magnitude, i.e., on the covalence of the tungsten-oxygen bond and the distortion degree of the [WO_6] octahedron. A similar transition 1*s*(Mo) $\longrightarrow$ 4*d*(Mo) + 2*p*(O) is observed at the molybdenum *K* edge. Its intensity is governed by the same factors as the intensity at the tungsten L_1 absorp-

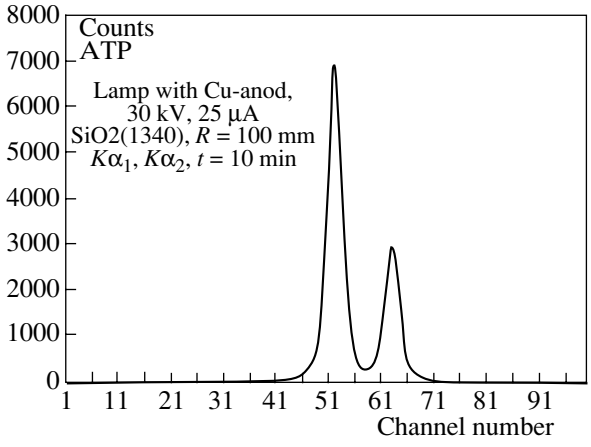

Fig. 31. The Cu K_{α_1} and K_{α_2} x-ray spectrum from a tube with a copper anode. The operating voltage and current are 30 kV and 25 μA, respectively, dispersing agent is SiO_2 (1340), R = 100 mm, t = 10 min.

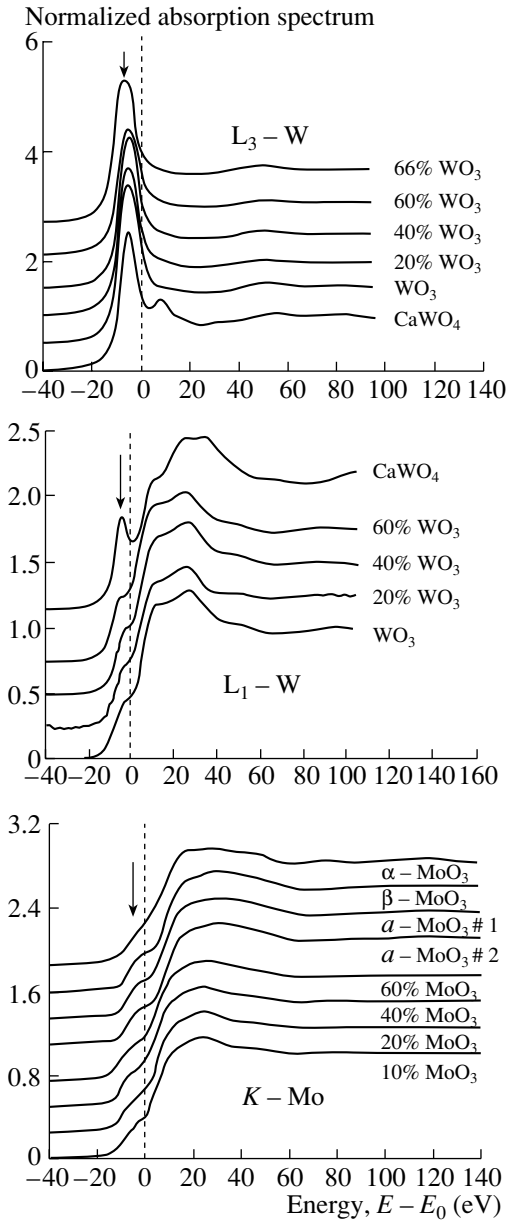

Fig. 32. The normalized XANES spectra of the tungsten (a) L_1 and (b) L_3 absorption edges and (c) molybdenum K absorption edge in barium-tungsten-phosphorus and calcium-molybdenum-phosphorus glasses, respectively. The vertical arrows are the white-line positions. The intensity of the white line at the L_1 and K edges increases with increasing distortion of the [MeO_6] octahedrons (Me stands for W or Mo).

tion edge. Thus, the intensity of the white line at the K and L_1 absorption edges can provide a qualitative conclusion on the distortion degree of the first coordination sphere of tungsten and molybdenum. As is seen from Fig. 32, comparison of the XANES signals from glassed and crystalline oxides of known structures suggests the distorted octahedral coordination of the tungsten (molybdenum) ions in glasses and amorphous films. This conclusion agrees well with the d^0 (W^{6+}, Mo^{6+}) electronic configuration of metal ions and with structure data that were obtained by analyzing EXAFS signals and will be presented below.

Figure 33 shows some of the EXAFS components extracted as described above and their Fourier transforms. The first peak, which is situated in the range from 0.8 to 2 Å, corresponds to the first coordination sphere and makes the dominant contribution, which is manifested as a dominant low-frequency signal in the experimental EXAFS component. More distant (>2 Å) peaks correspond to the contributions from the multiparticle distribution functions in the first coordination sphere and from the next coordination spheres. Quantitative analysis is virtually impossible because the contributions are numerous and their Fourier transforms strongly overlap. For this reason, only the contribution from the first coordination sphere of tungsten (molybdenum) will be discussed below.

For describing the displacement direction of a metal atom from the octahedron center, we use the following notation: ⟨100⟩, ⟨110⟩, and ⟨111⟩ are the displacements toward the vertex, link, and the center of the face of the [MeO_6] octahedron, respectively. This notation coincides with the crystallographic directions for cubic perovskite-like structure.

To obtain accurate structural data, the EXAFS signal from the first coordination sphere is analyzed within the framework of the convenient multicomponent Gaussian model and by the model independent method described above. Figure 40 shows the resulting RDFs and clearly demonstrates that the nearest oxygen atoms surrounding the tungsten atoms in the barium-tungsten-phosphorus glasses are divided into two groups, each of three atoms (3 : 3 division) at the distances 1.7 and 2.0 Å (see Fig. 34a). The wide peak at a distance of 1.3 Å is false (non-structure) contribution and is likely related to the oscillating component of the atomic absorption coefficient, i.e., the so-called atomic EXAFS signal (atomic XAFS) [98]. The observed division of the first coordination sphere of a tungsten atom corresponds to the displacement of the atom along the ⟨111⟩ direction toward the octahedron face. As the tungsten oxide WO_3 content in a glass becomes equal to or higher than 60%, the ratio of the intensities of two peaks in the RDF changes so that the more distant peak (at 2.0 Å) decreases. This change can be attributed to the fact that some tungsten atoms begin to displace along the ⟨110⟩ direction. In this case, the first coordination sphere of tungsten is divided into two parts containing four close and two distant oxygen atoms (4 : 2 division). We note that this distortion of the octahedron is similar to that observed in the crystalline WO_3. Under the assumption that two types of centers exist in the 60%-WO_3 glass, the ratio of the intensities of the peaks in the RDF indicates that 70% and 30% of [WO_6] octahedrons must be with the 3 : 3 and 4 : 2 distortions, respectively (see Table 5).

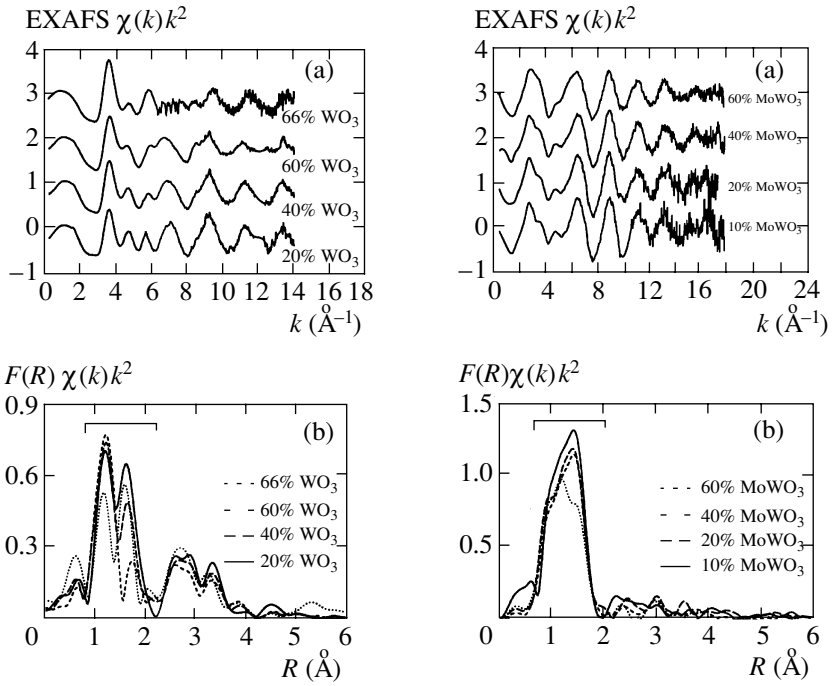

Fig. 33. (a) The EXAFS signals from the tungsten L_3 edge and molybdenum K edge in barium-tungsten-phosphorus and calcium-molybdenum-phosphorus glasses, respectively; (b) corresponding Fourier transforms $F(R)$. The first coordination sphere region is indicated in the Fourier transforms.

In the 66%-WO_3 tungsten-phosphorus glass free of the barium oxide, the first coordination sphere of tungsten is divided into two parts consisting of two and four oxygen atoms at distances of 1.7 and 2.0 Å, respectively. This distortion differs somewhat from that observed in glasses including barium oxide and can be explained by the double role of the tungsten oxide that participates both in formation of a glass frame and as a modifier oxide.

The distortion of [WO_6] octahedrons in the a-WO_3 amorphous film is larger than that in the crystalline WO_3. However, this distortion is similar to the latter in the type of division of W–O bonds into groups, which is consistent with the nanocrystalline structure of the films, and strongly differs from that in glasses with low tungsten-oxide content.

The results obtained for the calcium-molybdenum-phosphorus glasses (see Fig. 34c) attest to distortion similar to that in the barium-tungsten-phosphorus glasses. Nevertheless, the first coordination sphere of molybdenum is somewhat more strongly distorted in this case, which is manifested in the asymmetric shape of the distant peak in the RDF. For this reason, one can approximately regard that the local environment of molybdenum ions is divided into three atomic groups consisting of three, two, and one oxygen atoms at distances of 1.7, 2.0, and 2.1 Å, respectively.

As well as in tungsten-phosphorus glasses, the distortion of [MoO_6] octahedrons in glass differs from that in the crystalline, α-MoO_3 and β-MoO_3, and amorphous, a-MoO_3, films, where molybdenum atoms are displaced from the center along the ⟨110⟩ direction. In conclusion, we note that the type of distortion in the first coordination sphere of tungsten and molybdenum in glasses coincides with that found in the monophosphorus tungsten bronzes [98].

Table 5. Distortion Δ (with the accuracy ±0.001 Å) of the first coordination sphere of tungsten and molybdenum in the crystals of the corresponding oxides. The directions ⟨110⟩ and ⟨111⟩ correspond to the ion displacements from the octahedron center toward a link and the center of a face of the octahedron, respectively

Compound	Distortion type	Displacement direction of W or Mo ion	Δ, Å
$CaWO_4$	4		0.045
$Na_{0.66}WO_3$	6	⟨110⟩	0.048
WO_3	4 : 2	⟨110⟩	0.143
a-WO_3	4 : 1 : 1	⟨111⟩	0.154
20% WO_3	3 : 3	⟨111⟩	0.160
40% WO_3	3 : 3	⟨111⟩	0.156
60% WO_3	3 : 3 (~70%)	⟨110⟩	0.143
	4 : 2 (~30%)		
66% WO_3	2 : 4		0.145
α-MoO_3	2 : 2 : 2	⟨110⟩	0.204
β-MoO_3	4 : 2	⟨110⟩	0.171
a-MoO_3#1	4 : 1 : 1	⟨110⟩	0.187
a-MoO_3#2	4 : 1 : 1	⟨110⟩	0.184
10% MoO_3	3 : 2 : 1	⟨111⟩	0.181
20% MoO_3	3 : 2 : 1	⟨111⟩	0.176
40% MoO_3	3 : 2 : 1	⟨111⟩	0.172
60% MoO_3	3 : 2 : 1	⟨111⟩	0.164

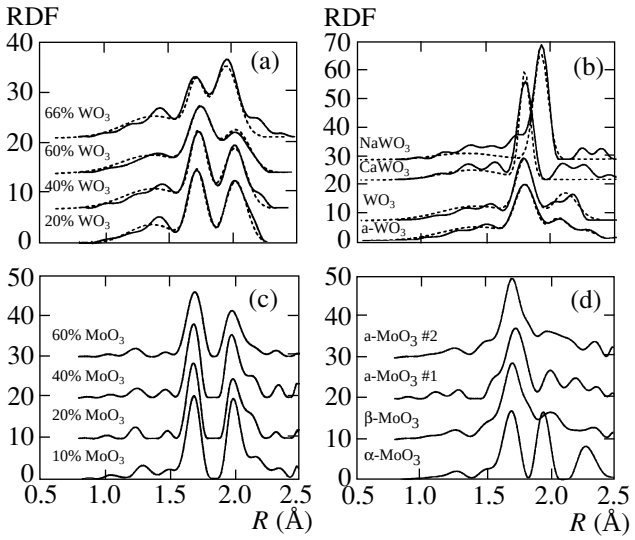

Fig. 34. The radial distribution functions (RDFs) around tungsten and molybdenum ions in $BaO–P_2O_5–WO_3$, $P_2O_5–WO_3$, and $CaO–P_2O_5–MoO_3$ glasses, in a-WO_3 and a-MoO_3 amorphous thin films, and in $CaWO_4$, $NaWO_3$, m-WO_3, α-MoO_3, and β-MoO_3 oxide crystalline compounds as calculated (solid lines) by model independent method and (dashed lines) in the framework of the multicomponent Gaussian model.

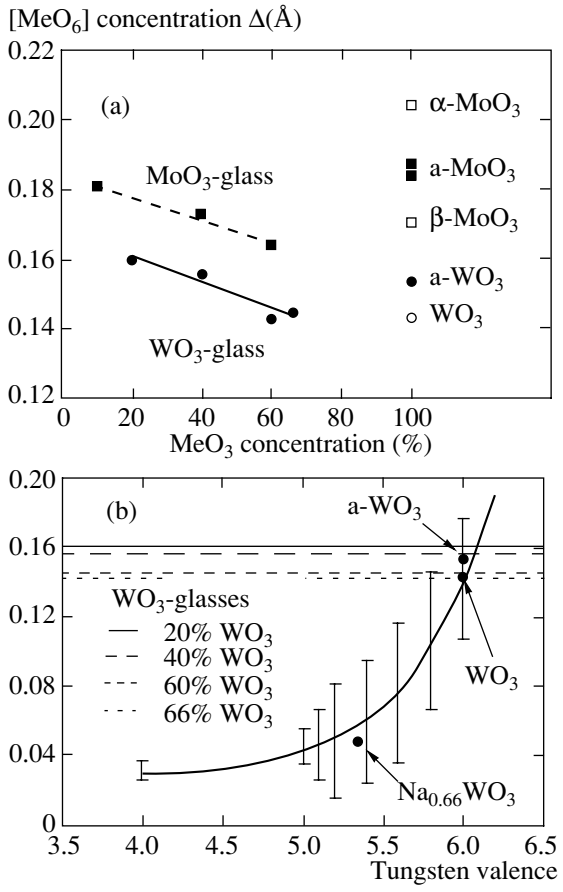

Fig. 35. The [MeO_6] octahedron distortion degree Δ (Me stands for W or Mo) as a function of (a) metal oxide concentration and (b) tungsten valence.

The degree of distortion of the [MeO_6] octahedron is quantitatively estimated by the formula $\Delta = \langle|R - \langle R\rangle|\rangle$ from the RDF. Table 5 presents the results. Figure 35b shows the dependence of the octahedron distortion degree on the tungsten ion valence [99]. The distortion degree Δ that is obtained by analyzing the EXAFS spectra for crystalline and amorphous $W^{6+}O_3$ agrees well with the observed dependence. For tungsten-phosphorus glasses, the calculated Δ value implies that most tungsten ions in the glasses are 6+ valent. Moreover, correlation between the octahedron distortion degree and the content of the metal oxide in the glass matrix was observed (see Fig. 35a). This indicates that the distortion of the metal-oxygen octahedron is determined not only by the electronic structure of the metal ion, but also by interactions caused by the matrix of a material [93].

Thus, considering the specific structure investigations of the oxide compounds of tungsten and molybdenum, we demonstrated that the method of the EXAFS spectroscopy at SR beams is highly efficient for studying the local electronic and atomic structures of absorbing centers.

6. INVESTIGATION OF THE STRUCTURAL FEATURES OF FULLERENES

Investigations of metal-doped fullerenes (fullerides) result in the appearance of a new field of physics. The phases A_xC_{60}, where A = Na, K, Rb, Cs and x = 1, 2, 3, 4, 6, were discovered. Special interest in the investigation of the physical properties of fullerene crystals was stimulated by the report about the observation of T_c = 10 K superconductivity in fullerene samples exposed within potassium vapors (K_3C_{60}). This phenomenon is related to the intercalation of potassium atoms to interstitial sites in the crystal lattice of a fullerene in complete analogy with graphite. Further investigations with various intercalated alkali metals lead to a change in T_c from 10 K for Na_2CsC_{60} to 31 K for Rb_2CsC_{60}. The occurrence of superconductivity in fullerene crystals is, in a certain sense, very interesting and exotic. Although the superconductivity mechanism is classical, there are certain peculiarities of the conduction band and vibrational modes.

Another class of fullerides AC_{60} with stoichiometric phases also exhibits a number of interesting properties. At high temperatures above 380 K, AC_{60} crystallizes into the fcc lattice of rock salt. Below 380 K, AC_{60} has two phases-stable polymer orthorhombic phase (*Pnnm*) [100] and metastable dimer monoclinic phase ($P2_1/a$) [101].

The polymer phase consisting of linear chains of C_{60} molecules, arises when a sample is slowly cooled, and is stable and conductive. On the other hand, the dimer phase arises from the high-temperature fcc phase when a sample is rapidly cooled and is nonconductive. The stable polymer phase exhibits a number of interesting physical properties. It has specific magnetic features and, at low temperatures, is unstable with regard to the

appearance of the spin (or charge) density wave. Rapidly cooling CsC_{60} and RbC_{60} to $T = 150$ and 125 K, respectively, Oszlanyi *et al.* [101] observed several metastable phases, one of which has a simple cubic structure with an unknown spatial group.

The SR x-ray diffraction results [100] unambiguously indicate that the second-order symmetry axis in the C_{60} molecule is directed along a direction in the crystal with the lattice constant $a = 9.13$ Å, and the C_{60} molecules are strongly deformed in the a direction, which leads to the appearance of the covalent-coupled structure. The specific π character of the intermolecular bonds in polymer chains is consistent with the conclusion that this material is a one-dimensional metal.

Another important problem of the structural analysis is to determine metal atom positions.

6.1. Subsystem of Alkali Metal Atoms

Below, we will consider the phase-transition structure changes induced in the subsystem of alkali metal atoms [102, 103].

Experimental data [100] indicate that a metal atom is in an octahedral environment of C_{60} molecules (see Fig. 36). The small radius of the alkali metal ion compared to the size of the octahedron consisting of large C_{60} molecules and strongly anisotropic Debye-Waller factors for a metal atom suggest that the true position of the metal atom differs from the central position shown in Fig. 36. In the general case, in the $Fm3m$ phase, the metal atom can take the following positions in the octahedral environment [104]: the central position 1*b* with the coordinate (111) and local O_h symmetry, the sextuple position 6*e* with the characteristic coordinate (00*z*) and C_{4v} symmetry, position 8*f* with (*xxx*) and C_{3v}, position 12*i* with (*xx*1) and C_{2v}, position 24*j* with (*xy*0) and C_s, and position 24*k* with (*xxz*) and C_s.

The metal atom in the 1*b* position can only oscillate around its equilibrium position. These displacements with the wave vector $\mathbf{k} = 0$ are transformed under the three-dimensional irreducible representation F_{1u} and, therefore, cannot be related with the secondary order parameters of the E_g or F_{2g} symmetry. Similar displacements with the wave vector (001) are transformed under the irreducible representations τ_4 and τ_{10} and also cannot be related with the order parameter $\xi_1 \neq 0$ of the τ_9 symmetry. Thus, any structural change with the metal atom at the octahedron center is absent in the phase transition.

When a metal atom takes the off-center position, the phase transition is accompanied by partial ordering in the positions shown in Figs. 36b, 36c, and 36d. The only secondary order parameter $\theta_2 \neq 0$ of the E_g symmetry in the 6*e* position describes the partial ordering of metal atoms either in the horizontal plane (closed circles) or in two positions above and below the plane (shaded circles). The secondary order parameters for positions 8*f* and 12*i* (Figs. 36c and 36d, respectively)

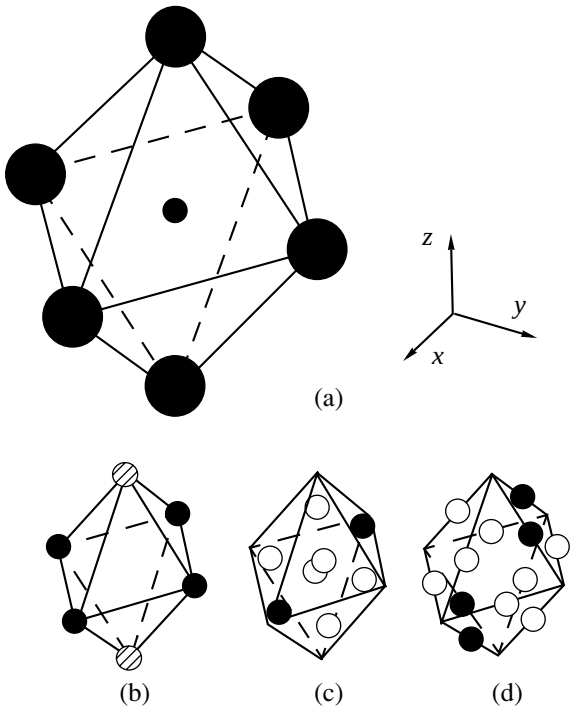

Fig. 36. Possible types of the positions of (small circles) metal atoms in the octahedral environment of (large circles) C_{60} molecules: (a) central 1*b*, (b) 6*e*, (c) 8*f*, and (d) 12*i* positions.

are $\eta_1 \neq 0$, $\xi_1 \neq 0$ and $\eta_2 \neq 0$, $\xi_2 \neq 0$, respectively. The closed circles are the occupied positions. Low-symmetry positions 24*j* and 24*k* arise from the positions 12*i* and 8*f*, respectively. The ordering of metal atoms in these positions is described by three secondary order parameters.

Therefore, we can assume that, with further decrease in temperature, the complete ordering of metal atoms can occur and the ordering phase transition leads to a lower crystal symmetry, which is completely determined by the position type. In particular, one of three possible variants of the complete ordering of metal atoms in the 8*f* position with the wave vector $\mathbf{k} = 0$ leads to the spatial group C_{2v}^7.

6.2. EXAFS Investigations of the Orthorhombic Phase in RbC_{60}

We consider the EXAFS-spectroscopy results for the metal atom positions in the RbC_{60} compound [105]. These measurements were carried out at the DESY SR source, Hamburg, by G. Wortmann *et al.* from Universität-GH Paderborn, Germany, with the participation of Yu.S. Grushko from the PNPI, Russia, to verify the theoretical predictions presented in the preceding section. A RbC_{60}-fulleride sample was preliminarily certified by using neutron and x-ray diffraction [106]. The lattice constant were found to be $a = 14.262$ Å, $b = 9.109$ Å,

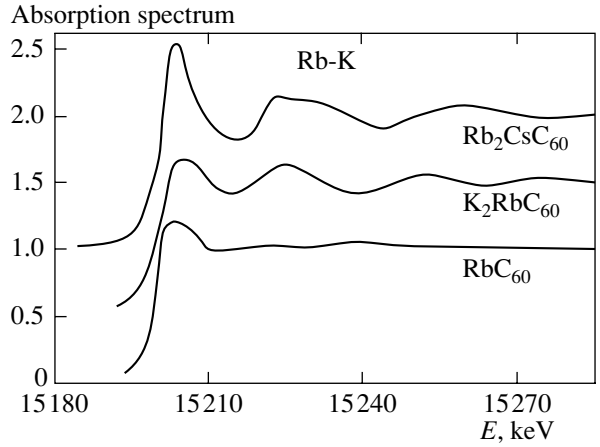

Fig. 37. The Rb *K* absorption edge spectrum from o-RbC_{60} and from superconductors Rb_2CsC_{60} and K_2RbC_{60}.

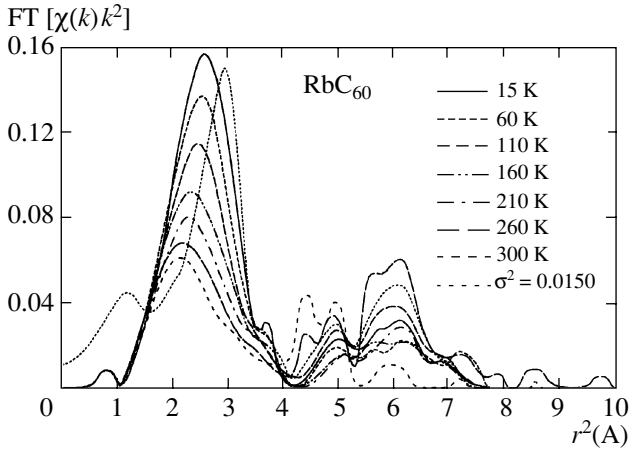

Fig. 38. The Fourier transforms (FTs) of the Rb EXAFS oscillations in RbO_{60} for various temperatures along with (dotted line) the theoretical result obtained for the central Rb position.

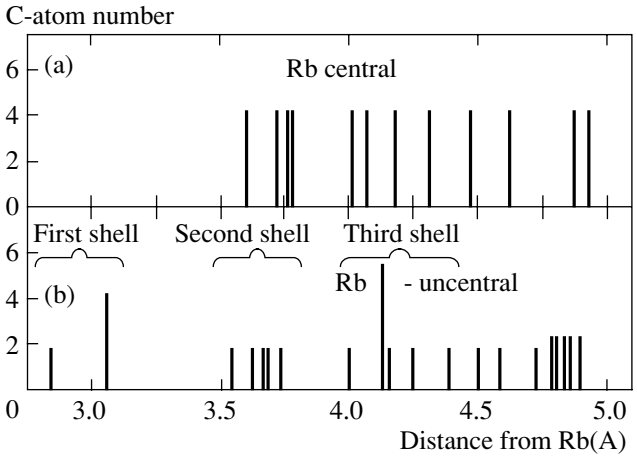

Fig. 39. Dash diagram of the Rb-C distances when Rb is (a) at the center of the octahedral interstitial sites and (b) in the off-center position (0.5, ε, ε), where ε = –0.07.

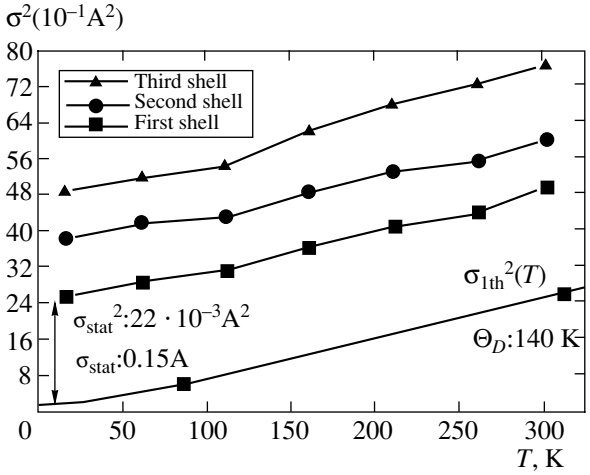

Fig. 40. Variances (triangles, circles, and squares) $\sigma^2_{1,2,3}$ of the radii of the nearest coordination spheres Rb-$C_{1,2,3}$, respectively, as a function of temperature *T*. The Debye-model is used for the approximation of the data.

and c = 10.120 Å. We were interested in the exact position of the Rb atom in the *o* phase. The possible off-center positions in this phase were mentioned in the x-ray diffraction measurements [106]. In corresponding cubic and superconducting systems A_3C_{60} and A_2BC_{60}, where A means K or Rb and B means Rb or Cs, systematic EXAFS studies determined the off-center positions of ions A and B in the octahedral environment [107].

The experiments were carried out with the ROMO-II beam in the temperature range from 15 to 300 K. Figure 37 shows the typical Rb *K* edge absorption spectrum for *o*-RbC_{60} in comparison with Rb_2CsC_{60}, where Rb takes exclusively tetrahedral (*T*) interstitial sites, and with K_2RbC_{60}, where Rb takes octahedral (*O*) interstitial sites. Both the edge structure and weak EXAFS oscillations attest to the Rb position with a low local symmetry for *o*-RbC_{60} and that the distribution of the nearest carbon atoms is similar to that for the Rb position in K_2RbC_{60} [17]. Figure 38 shows the Fourier transforms (FTs) of the Rb EXAFS oscillations for various temperatures along with the theoretical calculation of FTs with Rb-C distances obtained for the central Rb position in the *O* site by using theoretical scattering amplitudes and phase shifts [17]. The Rb-C distances are shown as a dash diagram in Fig. 39. Theoretical line distinctly differs from the experimental data in the maximum of the radial distribution function. This situation is similar to that in the *o*-site analysis [17]. The measured FT spectra was reasonably approximated with the off-center position (0.5, ε, ε), where ε = –0.07, and with the Rb-C distance distribution shown in Fig. 39b.

In previous EXAFS analysis, the inversely transformed spectra were approximated with three coordination spheres of carbon, which leads to the Rb-C distance distribution shown in 39b. Good approximation was obtained with Rb-C_1 = 3.08(2) Å, Rb-C_2 = 3.54(3) Å,

and Rb-C_1 = 3.90(5) Å. These distances were found to be almost temperature independent. The obtained distances were used as the input at the second stage of the analysis, which determined the variances of the distances. Figure 40 shows the variances $\sigma^2(T)$ of the Rb-C distances. The fitted Debye temperature of 140 K in the EXAFS method for the first coordination sphere well reproduces the strong temperature dependence of the EXAFS signal in Fig. 38. The relatively large static contributions $\sigma^2(T)$ reflect the Rb-C distance distribution shown in Fig. 39.

7. CONCLUSION

Because of the development of SR sources, the EXAFS spectroscopy method has become one of the basic methods for exploring the structure in amorphous quasicrystalline substances of various origins. This method is of great importance in application to nanostructures, such as quantum points, nanotubes, and fine-grained semiconductor structures. We emphasize the great demand for new materials for creating new medications. All these applications stimulate the development of precise analytical methods for studying microscopic amounts of substances.

The further advancement of EXAFS spectroscopy methods in application to kinetic processes in condensed matter is related to the use of third-generation high-intense SR sources, development of x-ray optics for obtaining x-ray beams of micron dimensions, and construction of two-dimensional detectors with high spatial resolution. Owing to the high cost of construction of spectrometers in SR beams, success can be achieved through wide cooperation between numerous research centers of various directions, from fundamental to industrial.

REFERENCES

1. See the Program Library of the European Synchronous Center ESRF in Internet: http://www.esrf.fr/.
2. Fricke, H., *Phys. Rev.*, 1920, vol. 16, p. 202.
3. Hertz, G., *Z. Phys.*, 1920, vol. 3, p. 19.
4. Coster, D., *Z. Phys.*, 1924, vol. 25, p. 83.
5. Lindh, A.E., *Z. Phys.*, 1921, vol. 6, p. 303; 1925, vol. 31, p. 210.
6. Ray, B.B., *Z. Phys.*, 1929, vol. 55, p. 119.
7. Kievit, B. and Lindsay, G.A., *Phys. Rev.*, 1930, vol. 36, p. 648.
8. Hanawalt, J.D., *Z. Phys.*, 1931, vol. 70, p. 20; *Phys. Rev.*, 1931, vol. 37, p. 715.
9. de L. Kronig, R., *Z. Phys.*, 1931, vol. 70, p. 317.
10. de L. Kronig, R., *Z. Phys.*, 1932, vol. 75, p. 468.
11. Peterson, H., *Z. Phys.*, 1932, vol. 76, p. 768; 1933, vol. 80, p. 528; 1936, vol. 98, p. 569.
12. Kostarev, A.I., *Zh. Eksp. Teor. Fiz.*, 1941, vol. 11, p. 60; 1949, vol. 19, p. 413.
13. Sawada, M., *Rep. Sci. Works Osaka Univ.*, 1959, vol. 7, p. 1.
14. Shmidt, V.V., *Izv. Akad. Nauk SSSR, Ser. Fiz.*, 1961, vol. 25, p. 977; 1963, vol. 27, p. 392.
15. Kozlenkov, A.I., *Izv. Akad. Nauk SSSR, Ser. Fiz.*, 1961, vol. 25, 957; 1963, vol. 27, p. 364; 1974, vol. 38, p. 500.
16. Sayers, D.E., Stern, E.A., and Lytle, W.F., *Phys. Rev. Lett.*, 1971, vol. 27, p. 1024.
17. Thole, T., Carra, P., Sette, F., and Van der Laan, G., *Phys. Rev. Lett.*, 1992, vol. 68, p. 1943.
18. Chen, C.T., Sette, F., Ma, Y., and Modesty, S., *Phys. Rev. B*, 1990, vol. 42, p. 7262.
19. Darty, E., Depautex, C., *et al.*, *Nucl. Instrum. Methods Phys. Res. A*, 1986, vol. 246, p. 452.
20. Kunz, C., *Synchrotron Radiation Techniques and Applications*, Kunz, C., Ed., Berlin: Springer, 1979, p. 1; Munro, I.H., Boardman, C.A., and Fuggle, J.C., *World Compendium of Synchrotron Radiation Facilities*, Orsay: ESRS, 1991.
21. Kincaid, B.M. and Eisenberg, P., *Phys. Rev. Lett.*, 1975, vol. 34, p. 1361.
22. *X-Ray Data Bookelet*, Vaughan, D., Ed., 1986.
23. *Synchrotron Radiation* (Proc. Thirtieth Scottish Universities Summer School in Physics), Greaves, G.N., Ed., Aberdeen, 1985.
24. *Synchrotron Radiation Research*, Winick, H., Ed., New York and London: Plenum, 1980.
25. Fontane, A., *School of the Use of Synchrotron Radiation in Science and Texnology*, Miramare Trieste, Italy, 1997.
26. Eisenberg, P. and Kincaid, B.M., *Chem. Phys. Lett.*, 1975, vol. 36, p. 134.
27. *X-Ray Absorbtion. Principle, Technique, Application of EXAFS, XANES, SEXAFS*, Köningsberger, P. and Prins, R., Eds., New York: Wiley, 1988.
28. Lindau, I. and Spicer, W.E., *J. Electron Spectrosc. Relat. Phenom.*, 1974, vol. 3, p. 409.
29. Beni, G. and Platzman, P.M., *Phys. Rev. B*, 1976, vol. 114, p. 1514.
30. Feldman, L. and Mayer, J., *Fundamentals of Surface and Thin Film Analysis*, New York: North-Holland, 1986.
31. Kuzmin, A., Mironova, N., Purans, J., and Radionov, A., *J. Phys.: Condens. Matter.*, 1995, vol. 7, p. 9357.
32. Kuzmin, A., Purans, J., Dalba, G., *et al.*, *J. Phys.: Condens. Matter.*, 1996, vol. 7, p. 9083.
33. Teo, B.K., *EXAFS: Basic Principles and Data Analysis*, Berlin: Springer, 1986.
34. Koningsberger, D.C. and Prins, R., *X-Ray Absorption: Principles, Applications, Techniques of EXAFS, SEXAFS and XANES*, New York: Wiley, 1988.
35. Kochubei, D.I., Babanov, Yu.A., Zamaraev, K.I., *et al.*, *X-ray Spectral Method to Study the Amorphous Body Structure: EXAFS Spectroscopy*, Novosibirsk: Nauka, 1988.
36. Kuzmin, A., *Physica B* (Amsterdam), 1995, vols. 208/209, p. 175.
37. Kuzmin, A., *J. Phys. IV*, 1997, vol. 7, p. C2-213.
38. Kuzmin, A., *EDA: EXAFS Data Analysis Software Package. User's Manual. Version 5.1*, Riga, 1999; Internet: http://www.dragon.lv/eda.

39. Vedrinskii, R.V. and Geguzin, I.I., *X-ray Absorption Spectra of Solid Bodies*, Moscow: Energoatomizdat, 1991.
40. Gurman, S.J., Binsted, N., and Ross, I., *J. Phys. C: Solid State Phys.*, 1984, vol. 17, p. 143.
41. Binsted, N. and Hasnain, S.S., *J. Synchrotron Radiat.*, 1996, vol. 3, p. 185.
42. Rehr, J.J., Mustre de Leon, J., Zabinsky, S.I., and Albers, R.C., *J. Am. Chem. Soc.*, 1991, vol. 113, p. 5135.
43. Rehr, J.J., Zabinsky, S.I., and Albers, R.C., *Phys. Rev. Lett.*, 1992, vol. 69, p. 3397.
44. Zabinsky, S.I., Rehr, J.J., Ankudinov, A., *et al.*, *Phys. Rev. B*, 1995, vol. 52, p. 2995.
45. Ankudinov, A.L., Ravel, B., Rehr, J.J., and Conradson, S.D., *Phys. Rev. B*, 1998, vol. 58, p. 7565.
46. Fillpponi, A., Di Cicco, A., Tyson, T.A., and Natoli, C.R., *Solid State Commun.*, 1991, vol. 78, p. 265.
47. Fillpponi, A., Di Cicco, A., and Natoli, C.R., *Phys. Rev. B*, 1995, vol. 52, p. 15122.
48. Filipponi, A. and Di Cicco, A., *Phys. Rev. B*, 1995, vol. 52, p. 15135.
49. Di Cicco, A., Rosolen, M.J., Marassi, R., *et al.*, *J. Phys.: Condens. Matter.*, 1996, vol. 8, p. 10779.
50. Kuzmin, A., Purans, J., Benfatto, M., and Natoli, C.R., *Phys. Rev. B*, 1993, vol. 47, p. 2480.
51. Kuzmin, A. and Grisenti, R., *Philos. Mag. B*, 1994, vol. 70, p. 1161.
52. Kuzmin, A. and Purans, J., *J. Phys.: Condens. Matter.*, 1993, vol. 5, p. 267.
53. Purans, J., Kuzmin, A., Parent, Ph., and Dexpert, H., *Physica B* (Amsterdam), 1995, vols. 208/209, p. 373.
54. Dalba, G., Diop, D., Fornasini, P., *et al.*, *J. Phys.: Condens. Matter.*, 1993, vol. 5, p. 1643.
55. Kuzmin, A., Obst, S., and Purans, J., *J. Phys.: Condens. Matter.*, 1997, vol. 9, p. 10065.
56. Kuzmin, A. and Purans, J., *J. Phys.: Condens. Matter.*, 1993, vol. 5, p. 9423.
57. Kuzmin, A. and Parent, Ph., *J. Phys.: Condens. Matter.*, 1994, vol. 6, p. 4395.
58. Kuzmin, A., Purans, J., and Parent, Ph., *Physica B* (Amsterdam), 1995, vols. 208/209, p. 45.
59. Purans, J., Kuzmin, A., Parent, Ph., and Laffon, C., *Ionics*, 1998, vol. 4, p. 101.
60. Kuzmin, A. and Purans, J., *Proc. SPIE*, 1997, vol. 2968, p. 180.
61. Kuzmin, A. and Purans, J., *J. Phys.: Condens. Matter.*, 1993, vol. 5, p. 2333.
62. Burattini, E., Purans, J., and Kuzmin, A., *Jpn. J. Appl. Phys., Suppl.*, 1993, vol. 32, no. 2, p. 655.
63. Balerna, A., Bernieri, E., Burattini, E., *et al.*, *Nucl. Instrum. Methods Phys. Res. A*, 1991, vol. 308, p. 234.
64. Stern, E.A., *Phys. Rev. B*, 1974, vol. 10, p. 3027.
65. Filipponi, A. and Di Cicco, A., *Phys. Rev. B*, 1995, vol. 51, p. 12322.
66. Bunker, G., *Nucl. Instrum. Methods Phys. Res. A*, 1983, vol. 207, p. 437.
67. Tranquada, J.M. and Ingalls, R., *Phys. Rev. B*, 1983, vol. 28, p. 3520.
68. Dalba, G., Fornasini, P., and Rocca, F., *Phys. Rev. B*, 1993, vol. 47, p. 8502.
69. Babanov, Yu.A., Vasin, V.V., Ageev, A.L. and Ershov, N.V., *Phys. Status Solidi B*, 1981, vol. 105, p. 747.
70. Ershov, N.V., Ageev, A.L., Vasin, V.V., and Babanov, Yu.A., *Phys. Status Solidi B*, 1981, vol. 108, p. 103.
71. Yang, D.S. and Bunker, G., *Phys. Rev. B*, 1996, vol. 54, p. 3169.
72. Kizler, P., *Proc. 6th Int. Conf. on X-ray Absorption Fine Structure, York*, Hasnain, S.S., Ed., Singapore: Ellis Horwood, 1991, p. 78.
73. Gurman, S.J. and McGreevy, R.L., *J. Phys.: Condens. Matter.*, 1990, vol. 2, p. 9463.
74. Bouldin, C.E. and Stern, E.A., EXAFS Studies of Amorphous Semiconductors, *EXAFS and Near Edge Structure III*, Hodgson, K.O., Hedman, B., and Penner-Hahn, J.E., Eds., Berlin: Springer, 1984, p. 273.
75. Stern, E.A., Ma, Y., Hanske-Petitpierre, O., and Bouldin, C.E., *Phys. Rev. B*, 1992, vol. 46, p. 687.
76. Teo, B.K. and Lee, P.A., *J. Am. Chem. Soc.*, 1979, vol. 101, p. 2815.
77. McKale, A.G., Veal, B.W., Paulikas, A.P., *et al.*, *J. Am. Chem. Soc.*, 1988, vol. 110, p. 3763.
78. Ruiz-Lopéz, M.F., Loos, M., Goulon, J., *et al.*, *Chem. Phys.*, 1988, vol. 121, p. 419.
79. Ruiz-Lopéz, M.F., Bohr, F., Filipponi, A., *et al.*, *Proc. 6th Int. Conf. on X-ray Absorption Fine Structure, York*, Hasnain, S.S., Ed., Singapore: Ellis Horwood, 1991, p. 75.
80. Tyson, T.A., X-ray Absorption Spectroscopy: Experimental K-, L- and KL-Spectra with Quantitative Models, *PhD Thesis*, Stanford Univ., 1991.
81. Dalba, G., Fornasini, P., Kuzrnin, A., *et al.*, *J. Phys.: Condens. Matter.*, 1995, vol. 7, p. 1199.
82. Stern, E.A., Theory of EXAFS, *X-Ray Absorption: Principles, Applications, Techniques of EXAFS, SEXAFS and XANES*, Koningsberger, D.C. and Prins, R., Eds., New York: Wiley, 1988, p. 3.
83. Filipponi, A., Di Cicco, A., Benfatto, M., and Natoli, C.R., *Europhys. Lett.*, 1990, vol. 13, p. 319.
84. Pustyl'nik, E.I., *Statistical Methods of Analysis and Processing of Observations*, Moscow: Nauka, 1968.
85. Tolentino, B., Darty, E., Fontone, A., *et al.*, *J. Appl. Crystallogr.*, 1988, vol. 21, p. 15.
86. Clarke, R., *Nucl. Instrum. Methods Phys. Res. A*, 1990, vol. 291, p. 117.
87. Aksenov, V.L., Ivanov, I.N., *et al.*, *Soobshch. Ob. Inst. Yad. Issled.* (Dubna), 1996, no. 314-96-502.
88. Andrault, D., Peryronneau, J., Farget, F., and Itie, J.P., *Physica B* (Amsterdam), 1995, vols. 208/209, p. 327.
89. Zhang, K., Dong, J., and Auld, D.S., *Physica B* (Amsterdam), 1995, vols. 208/209, p. 719.
90. Hatje, U., Hagelstein, M., Refler, T., and Forster, H., *Physica B* (Amsterdam), 1995, vols. 208/209, p. 646.
91. Kovalenko, M., Mironov, V., Shaliapin, V., and Tiutiunnikov, S., *J. Alloys Compd.*, 1999, vol. 286, p. 26.
92. Granqvist, C.G., *Handbook on Inorganic Electrochromic Materials*, Amsterdam: Elsevier, 1995.
93. Kunz, M. and Brown, I.D., *J. Solid State Chem.*, 1995, vol. 115, p. 395.

94. Bersuker, I.B., *Electron Structure and Properties of Coordination Compounds*, Leningrad: Khimiya, 1974.
95. Kuzmin, A. and Purans, J., *J. Phys. IV*, 1997, vol. 7, p. C2-971.
96. Kuzmin, A. and Purans, J., *Proc. SPIE*, 1997, vol. 2968, p. 180.
97. Rehr, J.J., Zabinsky, S.I., Ankudinov, A., and Albers, R.C., *Physica B* (Amsterdam), 1995, vols. 208/209, p. 23.
98. Labbe, P., Goreaud, M., and Raveau, B., *J. Solid State Chem.*, 1986, vol. 61, p. 324.
99. Domenges, B., McGuire, N.K., and O'Keeffe, M., *J. Solid State Chem.*, 1985, vol. 56, p. 94.
100. Stephens, P.W., Bortel, G., Faigel, G., *et al.*, *Nature*, 1994, vol. 370, p. 636.
101. Oszlanyi, G., Bortel, G., Faigel, G., *et al.*, *Phys. Rev. B*, 1996, vol. 54, p. 11849.
102. Aksenov, V.L., Ossipyan, Yu.A., and Shakhmatov, V.S., *Pis'ma Zh. Eksp. Teor. Fiz.*, 1995, vol. 62, p. 428 [*JETP Lett.* (Engl. Transl.), 1995, vol. 62, p. 439].
103. Aksenov, V.L., Ossipyan, Yu.A., and Shakhmatov, V.S., *J. Low Temp. Phys.*, 1997, vol. 107, p. 547.
104. Kovalev, O.V., *Irreducible and Induced Representations of the Fedorov Groups*, Moscow: Nauka, 1986.
105. Aksenov, V.L., Gieters, H., Grushko, Yu.S., *et al.*, *DESY-Annual Report*, Hamburg, 1998.
106. Launois, P. *et al.*, *Phys. Rev. Lett.*, 1998, vol. 81, p. 4420.
107. Nowitzke, G. *et al.*, *Phys. Rev. B*, 1996, vol. 54, p. 13230; *Mol. Cryst. Liq. Cryst.*, 1994, vol. 245, p. 321.

SPELL: OK